

平成 28 年度博士論文

博士（資源学）

Effects of eruption type on the genesis, transportation, and deposition
of some lahars

- volcanic phenomena induced by activities of subvolcanic
hydrothermal systems -

噴火様式の差異によるラハールの発生・流動様式への影響

-火山体直下熱水系の活動に起因する火山現象-

2017

南 裕介

Yusuke Minami

博士工 9514007

秋田大学大学院

工学資源学研究科博士後期課程

資源学専攻

ABSTRACT

Lahar is a hazardous volcanic phenomenon. The term of a lahar is defined as the flow of a water-saturated mixture of water and debris that moves down on flanks of volcanoes. The flow characteristic of a lahar is changed by mixing with surface water as they travel downstream. Aspects of the downstream dilution and the flow transformation are influenced by solid components. The downstream dilution occurs more readily in clay-poor lahars (or cohesionless lahars) than in clay-rich lahars (or cohesive lahars) because clay-poor lahars mix with external water competently. The clay components of the clay-rich lahars are typically derived from the hydrothermally altered volcanic edifices. The compositional characteristic, which is a clue to the origin of lahars, influence the flow behavior. To understand the behaviors including flow transformations, origin, and genesis of laharitic flow, we describe the lateral variations of sedimentary facies and the temporal variation in components for the lahar deposits at the northern base of Chokai volcano in this study. To consider the effects of activities of a subvolcanic-hydrothermal system on the occurrence of lahar, we investigated the mineralogy of the volcanic ash from the eruption at Ontake volcano on September 27, 2014, and compared with those of lahar deposits at the Chokai volcano.

Chokai volcano is an andesitic stratovolcano located in northeast Japan. There are volcanic-fan deposits at the northern base of Chokai volcano that overlie debris avalanche deposits. The volcanic fan gradient changes from steep to gentle with distance from the volcanic center. Microgeomorphology changes from lobate to smooth plain accordingly. The volcanic fan is composed of a series of post-collapse lahar deposits. The lahar deposits were emplaced as debris flow and hyperconcentrated flow mostly in the proximal volcanic fan, whereas the distal volcanic fan mostly comprises streamflow lahar facies and fluvial deposits, accompanying minor debris flow and hyperconcentrated flow facies.

This spatial variation implies that lahars flowed down as debris flows in proximal area; then, they transformed into stream flows, although some debris/hyperconcentrated flows reached to the distal area. The facies variation reflects geomorphology of the volcanic fan; the debris flow deposits in the steep proximal volcanic fan form debris flow lobes, and the streamflow deposits form a gentle smooth plain in the distal volcanic fan. After the deposition of the debris avalanche 2.5 ka, lahar reached to the volcanic fan at least four times: the 4th – 6th century BC, 5th – 7th century AD, 8th-12th century AD, and 1801 AD. More debris flows arrived in the proximal volcanic fan, during mostly just after the emplacement of debris avalanche.

The volcanic ash of the eruption on 27th September 2014 at Ontake volcano consists mostly of altered rock fragments. The ash contains partly altered volcanic rock fragments consisting of primary igneous minerals (plagioclase, orthopyroxene, titanomagnetite, and feldspars) and volcanic glass accompanied by alteration minerals to some extents, and contains no juvenile fragments. These features indicate that the eruption was a non-juvenile hydrothermal eruption that was derived from the hydrothermal system developed under the crater. The major minerals derived from hydrothermal alteration zones are silica mineral, kaolin group mineral, smectite, pyrophyllite, muscovite, alunite, anhydrite, gypsum, pyrite, K-feldspar, albite, and rutile. Minor chlorite, biotite, and garnet are accompanied. Five types of alteration mineral associations are identified from observations on individual ash particles; silica - pyrite, silica - pyrite \pm alunite \pm kaolin, silica - pyrophyllite - pyrite, silica - muscovite \pm chlorite, and silica - K-feldspar \pm albite \pm garnet \pm biotite. The associations indicate development of advanced argillic, sericite, and potassic alteration zones under the crater. The occurrence of anhydrite veinlet and the set of alteration zones indicate hydrothermal alteration zones similar to late-stage porphyry copper systems. Comparing the mineral associations with the geologic model of the late-stage porphyry copper systems, the source depths of mineral associations are estimated

to range from near surface to >2 km. The depths of advanced argillic alteration, sericite, and potassic zones are 0 to ~2 km, ~1.5 to ~2 km, and >2 km, respectively.

Genesis of the lahar deposits at the northern base of Chokai volcano was inferred from their volumes, componential features, and historical documents. The muddy lahars occurred after the sector collapse in 466 BC. Series of sandy lahars followed the event of muddy lahar in the period between 5th to 9th centuries AD. Then, a muddy lahar took place in 1802 AD. The first lahar event was induced by the sector collapsed, and the sandy lahars in the next stage are attributed to magma eruptions. The final lahar event was caused by a hydrothermal (or phreatomagmatic) eruption. The facies variations imply the transformation from debris flow to hyperconcentrated flow (or sheetflood), preserved in both of muddy and sandy lahar deposits. Stratification of the hyperconcentrated flow (and sheetflood) deposits overlying the debris flow deposits indicate that flow transformation can occur even in muddy flow.

CONTENTS

ABSTRACT.....	1
CONTENTS.....	4
CHAPTER I. INTRODUCTION.....	7
CHAPTER II DEPOSITIONAL PROCESSES AND TEMPORAL COMPONENT – CHANGE OF LAHAR DEPOSITS AT THE NORTHERN FOOT OF CHOKAI VOLCANO, NE JAPAN	10
2.1. Introduction.....	10
2.2. Geological and geographical setting.....	12
2.3. Observation object and methods.....	16
2.4. Geomorphology of the volcanic fan.....	17
2.5. Sedimentary facies analysis.....	23
2.6. Facies change from proximal to distal areas.....	36
2.6.1. Proximal area.....	36
2.6.2. Medial area.....	36
2.6.3. Distal area.....	37
2.7. Minerals in the lahar deposits.....	37
2.8. Carbon 14 dating.....	39
2.9. Discussion.....	41
2.9.1. Depositional processes of fan deposits.....	41

2.9.2. Relationship between geomorphology and distribution of lahar deposit.....	42
2.9.3. Temporal component –change of Lahar Deposits.....	43
2.9.4. Correlation between lahar events and eruptive history.....	44
2.10. Conclusion.....	46
CHAPTER III. MINERALOGICAL STUDY ON VOLCANIC ASH OF THE ERUPTION ON 27TH SEPTEMBER 2014 AT ONTAKE VOLCANO, CENTRAL JAPAN: CORRELATION WITH PORPHYRY COPPER SYSTEMS.....	47
3.1. Introduction.....	47
3.2. Geological setting of Ontake volcano.....	48
3.3. The 2014 eruption.....	48
3.4. Sampling and Methods.....	49
3.5. Results.....	51
3.5.1. Minerals in the ash.....	51
3.5.2. Mineralogy and petrography of individual ash grain.....	54
3.5.2.1. Partly altered volcanic rock fragment.....	58
3.5.2.2. Silica mineral – pyrite.....	58
3.5.2.3. Silica mineral - pyrite ± alunite ± kaolin-group mineral.....	59
3.5.2.4. Silica minerals - pyrophyllite – pyrite.....	61
3.5.2.5. Silica minerals – muscovite.....	61

3.5.2.6. Silica minerals - K-feldspar ± albite ± garnet ± biotite.....	61
3.5.2.7. Crystals of pyrite, anhydrite, and gypsum.....	62
3.5.3. Compositional variations in alunite crystals.....	62
3.6. Discussion.....	63
3.7. Conclusions.....	69
CHAPTER IV. DISCUSSION.....	71
CHAPTER V. CONCLUSIONS.....	76
REFERENCES.....	78
ACKNOWLEDGEMENTS.....	93
APPENDICES.....	94

CHAPTER I. INTRODUCTION

The term of “lahar” means a general term for a rapidly flowing mixture of rock debris and water from a volcano (Smith and Fritz, 1989; Vallance and Iverson, 2015). Some of serious volcanic hazards were directly caused by lahars, for example, Mt. Pinatubo in the Philippines in 1991 (Vallance, 2000), Nevado del Ruiz in Columbia in 1985 (Vallance, 2000), and Tokachidake volcano in Japan in 1926 (Uesawa, 2014). Lahars occurred in last century killed more than 30,000 peoples in the world (e.g. Schmincke, 2004; Vallance and Iverson, 2015), therefore understanding the nature of lahar is needed to prevent and reduce the lahar disaster.

Lahars commonly change character as they travel downstream (Vallance and Iverson, 2015). Lahars, which typically move faster than normal streamflow, push river water ahead of them and gradually, with distance downstream, begin to mix with that water (Pierson and Scott, 1985; Cronin et al., 1997). Such downstream dilution and flow transformation of lahars can be affected by their components. The process of downstream dilution occurs more readily in clay-poor lahars (or cohesionless lahars) than in clay-rich lahars (or cohesive lahars) because clay-poor lahars mix more readily with water (Vallance, 2000). In clay-poor lahars occurred at Mount St Helens in 1980 and 1982, downstream dilution occurred over the course of tens of kilometers and caused a complete transformation from debris flow to hyperconcentrated flow (Vallance, 2000; Vallance and Iverson, 2015). On the other hands, clay-rich lahar depositions at Mount Rainier reflect deposition solely from debris-flow phases (Vallance, 2000).

Clay components of clay-rich lahars are typically derived from hydrothermally altered volcanic edifice, because of clay-rich sediments are both uncommon on the flanks or aprons of active volcanoes (Vallance and Iverson,

2015). Clay-rich lahar deposits commonly contain altered volcanic rocks consisting fine-grained silica phases and clay minerals, such as kaolinite and smectite (e.g. Mount Rainier: Vallance and Scott, 1997; John et al., 2008; Mount Baker: Frank, 1983; Proto-Tongariro volcano: Lecointre et al., 2002; Adataara volcano: Yamamoto, 1998; Tokachidake volcano: Uesawa, 2014; Yakeyama volcano: Ohba et al., 2007; Citlaltépetl volcano: Carrasco-Núñez et al., 1993; Nevado de Colima volcano: Capra and Macías, 2002; Nevado de Toluca volcano: Capra and Macías, 2000; Iliamna Volcano: Waythomas et al., 2000). It is generally referred to as clay-rich lahars are induced by collapses of hydrothermally altered volcanic edifice (Vallance and Iverson, 2015), as reported in many volcanoes (Mount Rainier: Vallance and Scott, 1997; Mount Baker: Frank, 1983; Nevado de Colima volcano: Capra and Macías, 2002; Nevado de Toluca volcano: Capra and Macías, 2000).

Whereas, some of clay-rich lahars are not induced edifices collapses, but spouted directly from craters formed by hydrothermal or phreatomagmatic eruptions. The term of “syneruptive-spouted type lahar” refers lahars caused by water released these craters (Sasaki et al., 2016). The syneruptive-spouted type lahars have been documented from the 2014 eruption of Ontake volcano (Sasaki et al., 2016), the 2000 eruption of Usu volcano (Mizugaki, et al., 2001; Hirose et al., 2007), the 2006 eruption at Meakandake volcano (Sasaki et al., 2006), the 2015 eruption of Hakone volcano (Mannen et al., 2015), and the 1997 eruption of Akita Yakeyama volcano (Ohba et al., 2007). These syneruptive-spouted type lahars relate activities of subvolcanic-hydrothermal system.

Componential characteristics of lahars are largely influenced by their causes and affect their flow behavior. To understand laharitic flow behavior including flow transformations, origin, and triggering mechanisms, thus, the descriptions of aspects from sedimentology and material science are needed. In this study, we describe lateral sedimentary facies change and temporal

components change of lahar deposits at the northern base of Chokai volcano, and discuss their flow transformations, triggering mechanism, and origins. To discuss the effects from activities of subvolcanic-hydrothermal system to lahar causes, we described the mineralogy of the volcanic ash from the eruption at Ontake volcano on September 27, 2014 and compared with those of lahar deposits at the Cholai volcano.

CHAPTER II.

DEPOSITIONAL PROCESSES AND TEMPORAL COMPONENT— CHANGE OF LAHAR DEPOSITS AT THE NORTHERN FOOT OF CHOKAI VOLCANO, NE JAPAN

2.1. Introduction

Lahar, a rapidly flowing debris-water mixture from a volcano, comprises debris flow, hyperconcentrated flow, flood flow, and streamflow in respect to flow regime (Smith and Fritz, 1989; Smith and Lowe, 1991; Vallance and Iverson, 2015). Flow regime of lahars changes when they travel downstream by mixing with surface water (Pierson and Scott, 1985; Cronin et al., 1997; Vallance and Iverson, 2015). As sedimentary facies of lahar deposit reflects the flow regime at a given location, the transformation of the flow relates to the spatial distribution of sedimentary facies (e.g. Scott, 1988; Smith, 1988; Smith and Lowe, 1991). The flow types and resulting facies are also related to the surface geomorphology of the deposits. A spatial variation of the geomorphology of depositional surface of lahar reflects the transformation of the flow too. Therefore, a study combining geology and geomorphology on a broad area including proximal and distal areas provides an insight into the conversion of lahar flow with distance.

Some former workers studied geomorphology of lahar deposit in different scales. In small scales, for example, debris flow part of lahar form lobes and levees when it deposits (Suwa and Okuda, 1983; Pack, 2005). In larger scales, many studies reported that volcanic fan and volcanoclastic apron are composed, at least partly, of lahar deposits (Suwa and Okuda, 1983; Smith, 1991; Smith and Lowe, 1991; Lavigne and Suwa, 2004). The gradually flattening concave slope of volcanic fans may relate to the flow type that changes with distance. The surface gradient of a deposit reflects the flow behavior of lahar, according to some

previous studies (Mizuyama, 1981; Rodolfo, 1989; Vallance and Scott, 1997); however, their results are applicable only to debris flow but not to more diluted, transformed flows which occur in distal areas. Therefore, the relationship between geomorphological association and the flow transformation of a lahar on a distal volcanic fan is unclear yet.

Geological and geomorphological investigations on lahar deposits in a volcanic fan also enable us to establish the evolutionary history of the fan and eruptive history of the volcano potentially. An involvement of the geology of a volcanic fan can elicit a more detailed eruptive history than the independent study around the near-vent area. Because proximal pyroclastic deposits on a high-relief volcano can be degraded easily or hidden by younger overlying pyroclastics, it is often difficult to establish the volcanic history from a geological observation on proximal pyroclastics alone (Kataoka et al., 2015). On the other hand, static distal fan can have a high potential of preservation of volcanic deposits, such as plinian tephra on floodplains. Lahar is one of such far-reaching volcanic products (e.g. Smith, 1988; Sohn et al., 1999). Stratigraphy of the distal area including lahar deposits complements a record of depositional packages reflecting periods when volcanic activity produces the debris. Organic matters tend to accumulate in such static environments under moist climates, intercalating with volcanic deposits. Then, ^{14}C dating can be applied to determine ages of the volcanic events. If past witnesses archived a volcanic event, comparison of the radiocarbon age and the document specifies which deposits is correlated with the event.

This study focusses on a lahar-dominated volcanic fan developed at the northern base of Chokai volcano, northern Honshu, Japan. The proximal part of the fan is composed of deposits accumulated by a series of debris flow and hyperconcentrated flow, resulting in peculiar geomorphological features such as debris flow lobes (Minami et al., 2015). However, the previous study excluded either of geology and geomorphology of the distal fan. This study aims to clarify

the relationship between flow transition of lahar and geomorphologic disposition by observing the entire volcanic fan of Chokai volcano including the distal part. Additionally, we establish the history of volcanic activities that related the evolution of the volcanic fan.

2.2. Geological and geographical setting

Chokai volcano ($39^{\circ} 05' 57''$ N, $140^{\circ} 02' 56''$ E; 2236 m above sea level) is a basaltic-andesitic stratovolcano, located in northern Honshu Island, Japan (Fig.2.1). The volcano comprises two edifices, East Chokai and West Chokai, both consisting mostly of lava flows (Hayashi, 1984). The volcanic edifices overlie Pleistocene-Pliocene sediments (Fig.2. 2: Hayashi, 1984; Ohzawa et al., 1982; Nakano and Tsuchiya, 1992).

The volcanic activity is divided into three stages. During Stage 1 (ca.600 – ca.160 ka), an ancestral edifice was built up by effusion of lava flows (Hayashi, 1984; Nakano and Tsuchiya, 1992; Ban et al., 2001), and then collapsed at least four times, resulting in the Yurihara debris avalanche deposit (YDA) on the Nikaho hill at the northern base of the volcano (Ohzawa et al., 1982; Hayashi, 1984; Nakano and Tsuchiya, 1992). During Stage 2 (ca.160 – ca.20 ka), andesitic lava flows effused from scattered vents, accompanying minor pyroclastic flow (Hayashi, 1984). The edifice of West Chokai was completed in this stage (Hayashi, 1984; Nakano and Tsuchiya, 1992; Ban et al., 2001). The last activity, Stage 3, commenced ca.20 ka and the latest activity is a phreatic or phreatomagmatic eruption in 1974 (Ban et al., 2001; Ui and Shibahashi, 1975). During this stage, a stack of lava flows effused to form the edifice of East Chokai volcano, while minor lava flowed from West Chokai (Hayashi, 1984; Nakano and

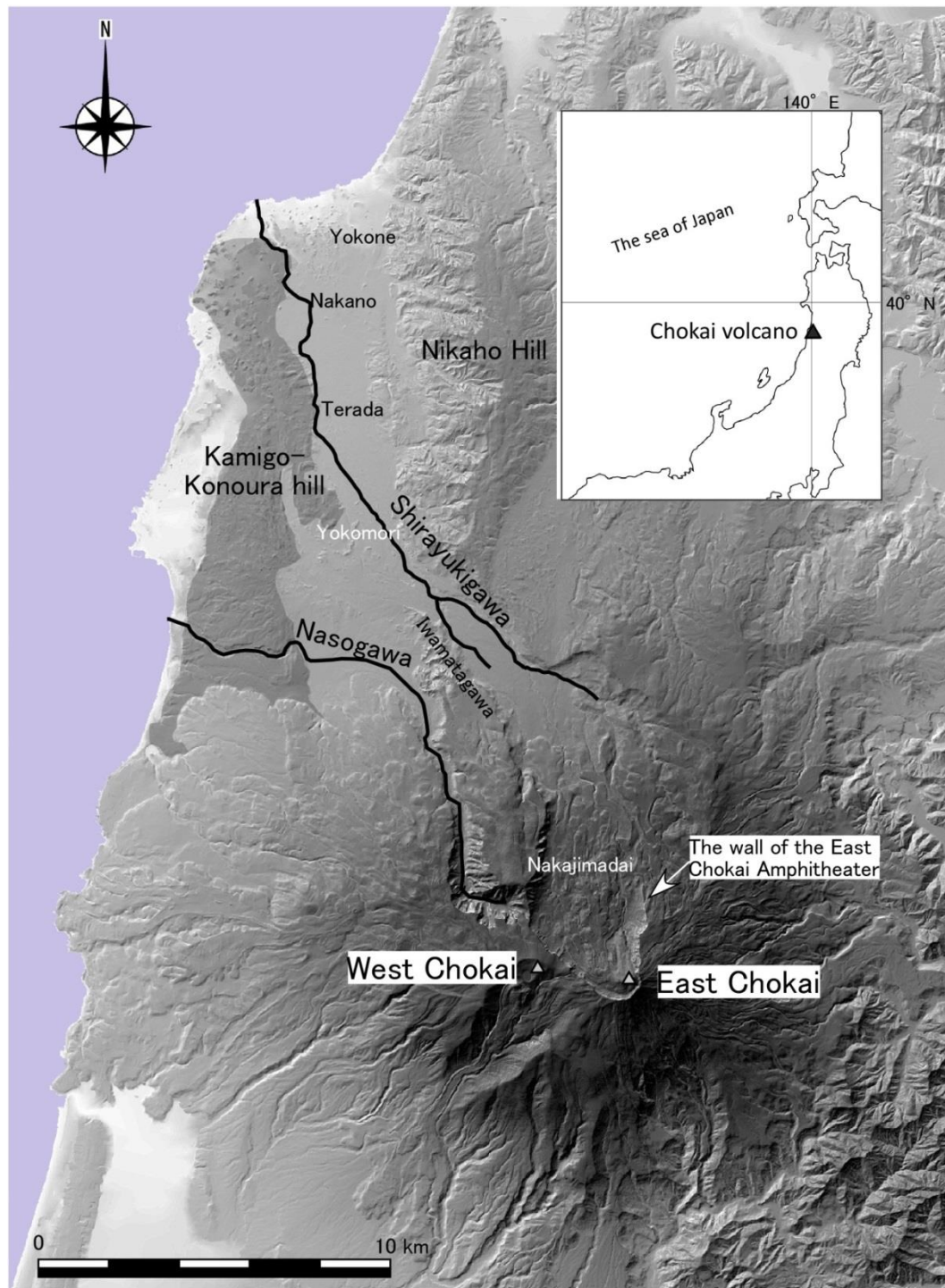


Fig.2.1 Map showing the geomorphology of the northern foot of Chokai volcano. The inset shows the location of the volcano. The topographic relief map is created from the 10m-mesh DEM data provided by the Geospatial Information Authority of Japan.

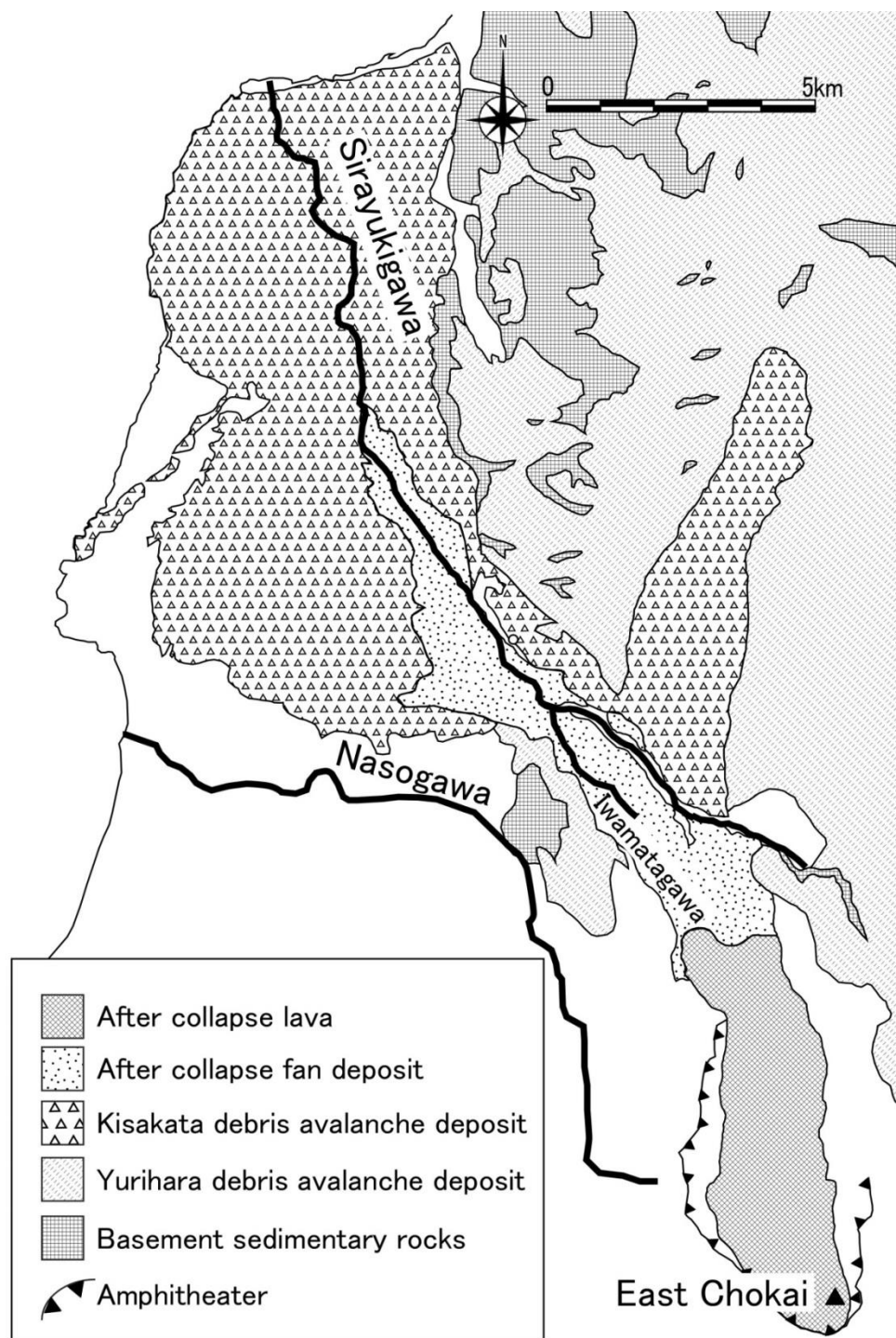


Fig. 2.2 Geological map of the northern base of Chokai volcano after Ohzawa et al. (1982).

Tsuchiya, 1992; Ban et al., 2001). The East Chokai edifice last collapsed BC466 (Mitsutani, 2001), leaving an amphitheater on the northern flank and Kusakata debris avalanche deposit (KDA) northwestward. After the collapse, a 0.8 km³ of lava pile emplaced within the amphitheater (Hayashi, 1984; Nakano and Tsuchiya, 1992). The summit lava dome (Shin-zan) located in the amphitheater, was formed by the latest magmatic eruption of 1800-1804 activities (Nakano and Tsuchiya, 1992). Minami et al. (2015) described lahar deposits of Stage 3 on the northern base. The study was carried out in the upper part of volcanic fan, where lahar deposits occur as debris flow and hyperconcentrated flow facies. However, the lahar deposits were poorly described in distal area, or the bottom fan area, because of limited exposures. This study represents new geological data from distal area obtained by excavation.

Broad geomorphology of the northern base of Chokai volcano is controlled by an NS-trending deformation structure of Neogene sediments (Ohzawa et al., 1982). The tectonic deformation of the Neogene sediments resulted in a set of N-S orientated rises at the north of the volcano: Nikaho hill, a 200-500-m-high plateau, and Kamigo-Konoura hill, a rise inclined to the north with a maximum height of 200 m in the south (Fig.2.1; Ohzawa et al., 1982, 1988). A volcanic fan is developed along the Shirayukigawa river system between Nikaho hill and Kamigo-Konoura hill. In the river system, rivers flow northwestward. The headstream of the river system comprises the drainage system in the amphitheater. The geology along the Shirayukigawa river system consists of KDA deposit and the post-collapse sediments including lahar deposits (Fig. 2.2; Ohzawa et al., 1982; Nakano and Tsuchiya, 1992; Minami et al., 2015). Hummocky hills of KDA are numerous distributed to the north of the volcanic fan (dense hummocky hills in Fig. 5) and on the Nikaho hill and on Kamigo-Konoura hill. The hummocky hills are also distributed within the volcanic fan but their density is sparser.

2.3. Observation object and methods

We carried out geomorphological analysis, geological survey, and ^{14}C geochronological dating of the volcanic fan. The geomorphology was analyzed on aerial photos taken by Geographical Survey Institute of Japan in 1976, and on a LiDAR map illustrated as the red relief image by Asia Air Survey Co., Ltd., provided through the courtesy of the Shinjo Office of River, Tohoku Regional Bureau, Ministry of Land, Infrastructure, Transport, and Tourism. The aerial photos were taken in 1976 whereas the laser measurement for the LiDAR was carried out in 2009. Comparison between these images with different ages enabled us to evaluate modern artificial modification of landscape.

Facies and stratigraphy of deposits were observed at outcrops and 12 excavation sites. The excavations down to 2 m depth were done by hand shovels for shallow part and coring with a flat hand-corer, Geoslicer (Takada et al. 2002). The deposits were classified into 12 types of sedimentary facies based on their sedimentary and compositional features. On the premise that each facies is ascribed to a specific regime of flow, we interpreted mechanisms of transportation and deposition of each facies.

The 16 samples were sampled from matrix of lahar deposits (ND1-16) and analyzed with X-ray diffractometer (XRD). Minerals were identified with the XRD (Multiflex; Rigaku Corp.) installed at Akita University. Measurements were carried out at a rate of 1° per minute from 2° to 40° using a $\text{CuK}\alpha$ target X-ray tube with an acceleration voltage of 30 kV and a filament current of 16 mA. A randomly oriented sample and an oriented sample were prepared for each fraction. Ethylene glycol, HCl, and heating treatments were applied to all fractions to determine clay mineral species.

AMS ^{14}C dating was applied to 13 organic samples (eight plant fragments, four pieces of charcoal, and an organic sediment sample). Plant fragments and charcoals are preferentially sampled and if they are not contained, organic sediments are sampled for dating. Seven organic samples (four plant fragments,

two charcoals, and an organic sediment) were collected from lahar deposits, and six organic samples (three plant fragments and three charcoals) were collected from floodplain deposits. Organic samples from floodplain deposits were obtained from near contacts between floodplain deposits and lahar deposits. The samples were prepared by acid/alkali/acid (AAA), except for an organic sediment that was treated by the acid-washing (AW) method. The age determinations were performed at Japan Nuclear Cycle Development Institute Tono Geoscience Center (JAT) for ten samples and at Beta Analytical Inc. (Beta) for three samples. The ^{14}C ages were converted into calendar ages by using OxCal 4.2 (Bronk Ramsey, 2009) based on the database IntCal13 (Reimer et al., 2013).

2.4. Geomorphology of the volcanic fan

The volcanic fan is developed along the Shirayukigawa river system between the two rises, extending from Nakajimadai where is the end of the intra-amphitheater lava flow in the south to the shoreline in the north. Near the coastline, there are a marine terrace and a hilly area where the KAD hummocky hills are densely distributed. The hilly area is located between distal volcanic fan and the marine terrace along Shirayukigawa. A marine terrace is developed along the coastline. The fan reaches to the shoreline in the northeastern end. Isolated hummocky hills of KDA are sparsely distributed in the volcanic fan, insulated by the volcanic fan plain. Although they are spatially contained with the volcanic fan, they are excluded from the fan, as the hummocky hills have a different origin from the fan. Topographic characteristics of the volcanic fan vary with distance from the volcanic edifice. Surface gradient varies continuously to gentler with distance. As the broad morphology of the fan is gently concave-upward, the areas are defined by surface gradient; the proximal fan for $> 2^\circ$, the medial fan for $1 - 2^\circ$, and the distal fan for $< 1^\circ$. The topographic development of debris flow lobes varies by the area accordingly; the closer to the volcanic edifice, the more developed the lobes are.

The proximal volcanic fan is clearly bounded at Nakajimadai on the south

by the scarps of the amphitheater-filling lava from Chokai. The proximal volcanic fan extends along Shirayukigawa and is bordered on the east by the southern end of Nikaho hill, and on the west by the cliff of the lower amphitheater (Figs. 2.3 and 2.4). The average is about 2 - 3°. Some 10-m-wide gullies develop in a northwest-southeast direction. Several distinct lobes are distributed around the confluence of the Iwamatagawa brook and Shirayukigawa (Fig. 2.3). However, on other parts of the proximal fan, the first surface of potential lobes have been blurred by the erosion forming small gullies. The lobes orientate a northwest-southeast direction and have dimensions of 50 – 100 m in wide, <500 m long, and <10 m in relative height. Our previous facies observation revealed that debris flow deposit comprises the lobes (Minami et al., 2015).

The medial volcanic fan has a fanwise morphology spread out westward and northward from Yokomori hamlet (Figs. 2.4 and 2.5). The uppermost part has a surface inclination of about 2°, and the inclination gradually decreases toward lower part to about 1°, where is defined as the border with the distal fan. As the surface gradient varies gradually from proximal to distal, the topography is continuous at the boundaries between the areas. Debris flow lobes are diffuse and smaller than those in the proximal volcanic fan (Figs. 2.3 and 2.4). An average dimension of the lobes is <10 m wide and <5 m height. These lobes are preserved only near Shirayukigawa, because modern agricultural cultivation has faded other lobes.

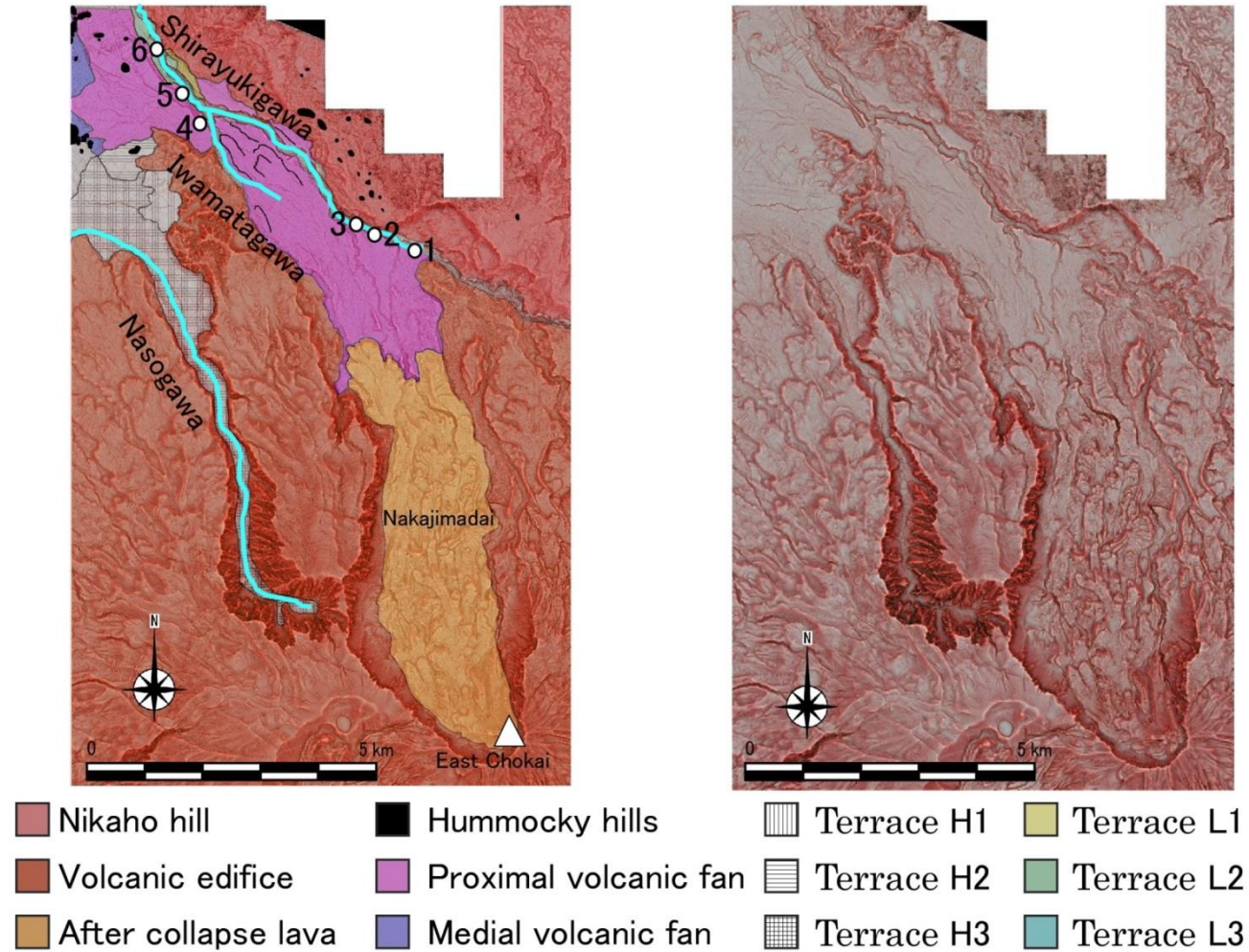


Fig. 2.3 The geomorphological map of the proximal volcanic fan. The base red relief image maps appearing hereinafter were produced by Asia Air Survey Co., Ltd. and provide d by the courtesy of Shinjo Office of River, Tohoku Regional Bureau, MLIT). The numbered open circles are the outcrop localities.

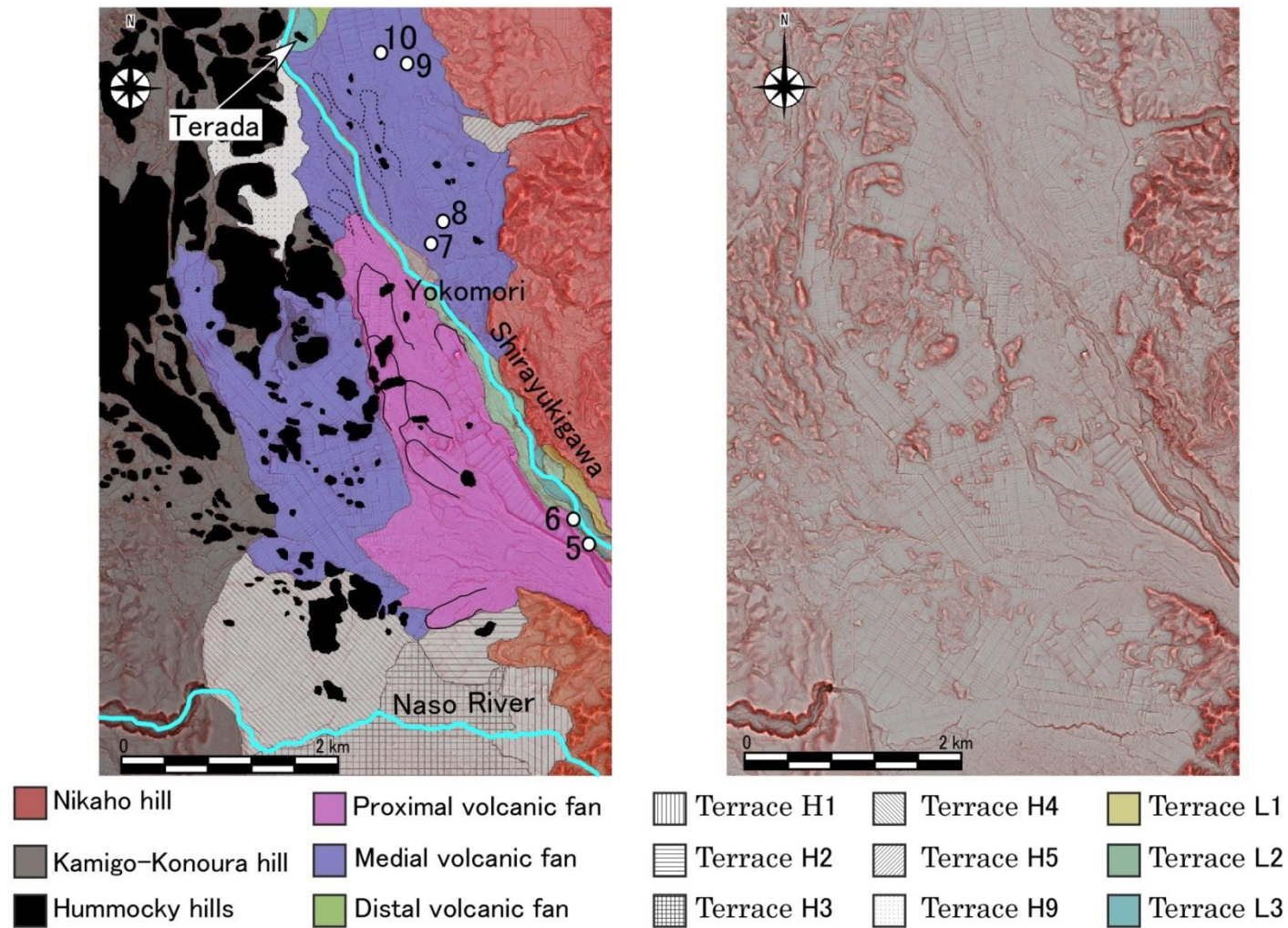


Fig. 2.4 The geomorphological map of the medial volcanic fan. The numbered open circles are the excavation sites in Figs. 5 and 6..

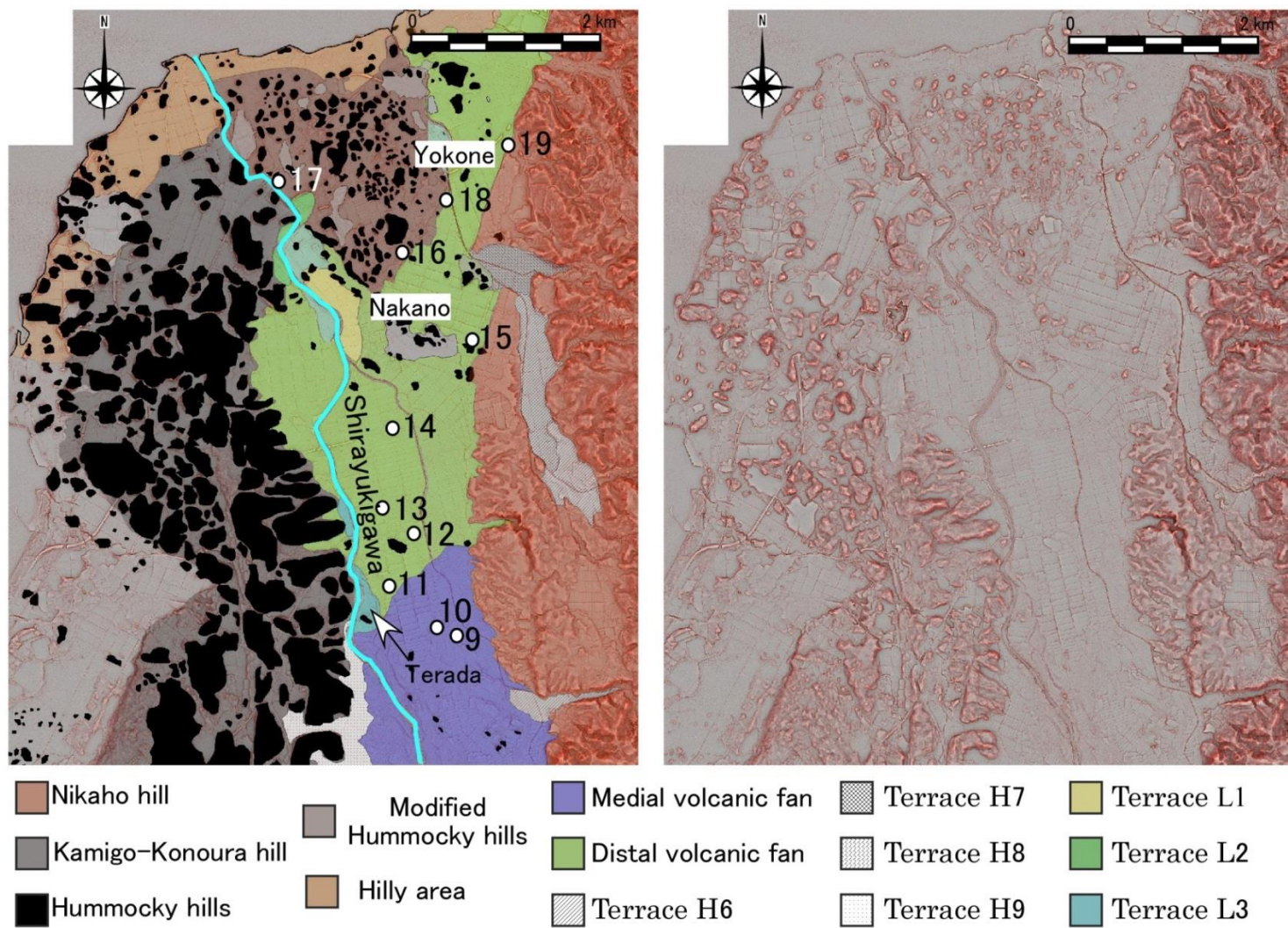


Fig. 2.5. The geomorphological map of the distal volcanic fan. The numbered open circles are the excavation sites in Figs. 5 and 6..

A flat surface characterizes the distal volcanic fan with a quite small gradient ($< 1^\circ$), where microgeomorphological features have been lost by artificial modification. Although agricultural development has blurred original topographic features, it is unlike that high-relief debris lobes were flattened to create a flat agricultural land because the scattered hummocky hills are intact there. Near the seashore, the distal volcanic fan is surrounded by two other distinct areas; the hilly area and the marine terraces (Fig. 2.5). The distal volcanic fan is bordered on the east by the base of the Nikaho hill, on the northwest by the Kamigo-Konoura hill, on the northwest by the hilly area, and on the northeast by the marine terrace.

There are ten river terraces located at levels higher than the volcanic fan, denoted as H1 – H10 in the order of level from high to low. The terraces H1 to H4 are distributed in the Nasogawa river system that is located in the adjacent to the Shirayukigawa river system (Figs. 2.1 and 2.4). The terraces H5 to H8 are located on the Nikaho hill and H9 on the Kamigo-Konoura hill. There are three terraces (L1, L2, and L3 in order from high to low) at the levels lower than the volcanic fan surface. The morphology of the low-level terraces, e.g. the terrace L3 in Terada hamlet (Fig. 2.5), has been artificially modified. These terraces are limitedly developed in the only vicinity of present Shirayukigawa. These fluvial terraces are distinguished from the volcanic fan by geomorphological features. The treads of terraces are even, whereas the fan has a concave-upward gentle surface. River systems are not developed on the treads, and the treads are separated from the fan or other terraces by the risers.

Hummocky hills are distributed in the medial and distal volcanic fan and hilly area and on Kamigo-Konoura hill and Nikaho hill. Distribution of hummocky hills varies in each area. Hummocky hills are so densely distributed that some of them connect each other in Kamigo-Konoura hill and hilly area. Otherwise, Hummocky hills are sparsely distributed in the medial and distal volcanic fan.

2.5. Sedimentary facies analysis

The volcanic-fan-forming deposits along the Shirayukigawa were observed at outcrops in the proximal volcanic fan (Loc. 1-6; Fig. 2.6) and 12 excavation sites (Loc. 7-19; Fig. 2.7) in the medial and distal volcanic fan. The fan deposits consist mainly of volcanoclastics or epiclastics with a matrix of syngeneic volcanic sand. These deposits are classified into 12 major sedimentary facies (Dmmm, Dmms, Dmcs, Dmcm, Dmbm, Dmbs, Gm, Sp, Ss, Sm, Fsm, C) based on their sedimentary features.

Facies Dmm: Matrix-supported massive diamicton with sandy (Dmms) or muddy (Dmmm) matrix

Description: Deposits of facies Dmm are characterized by matrix-supported gravels (Fig. 2.8A and 2.9A). The deposits are 20 to 800 cm thick in the proximal volcanic fan (Loc. 1-6; Minami et al., 2015) and 5 to 70 cm in the medial and distal volcanic fan (Loc. 7-19). The deposits are composed of particles with a broad range of size from fine to boulder. The maximum diameters of clasts are ~100 cm in the proximal volcanic fan and ~50 cm in the medial and distal volcanic fans. Majority of the gravels are composed of fresh andesite, ranging from pebble to boulder that are subrounded. The facies frequently contains gravels of altered volcanic rocks that show various colors from grayish blue to grayish white, indicating different degrees of alteration. Minor muddy rip-up clasts are contained too. Preferred clast orientations are present. The deposits are massive, poorly sorted, and lacking interstratification or clear grading, whereas coarse-tail normal grading from cobble to granule is rarely observed. Contacts with underlying deposits are clear and erosive, except for the transitional changes to Dmb.

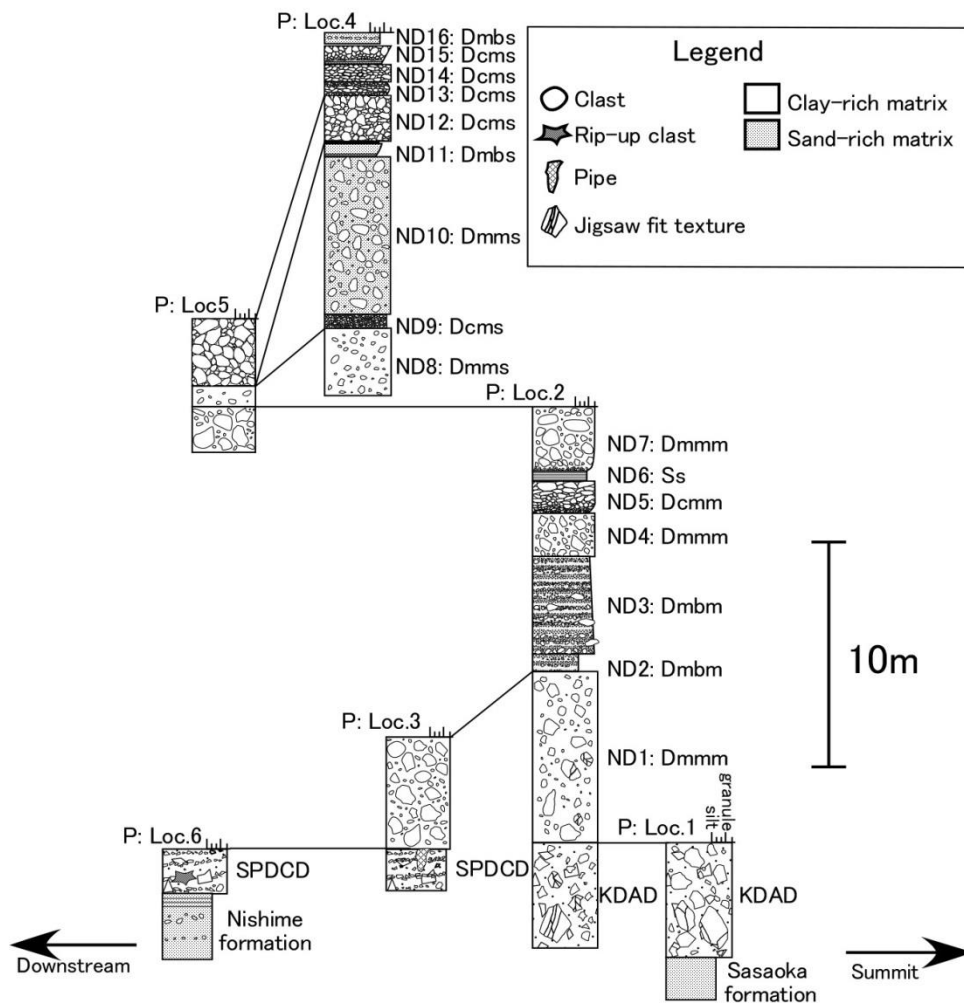


Fig. 2.6. Stratigraphic sections of the observed outcrops reported in the proximal volcanic fan, modified from Minami et al.(2015). The locations of outcrops are shown in Fig. 2.4. The Shirayukigawa pyroclastic density current deposit (SPDCD) and the Kisakata debris avalanche deposit (KDAD) are overlain by the volcanic fan deposits. The facies codes and unit names (ND1-16) are noted on the sections (see chapter 2.5). The codes beside the location number correspond to the area observed classified: P: the proximal volcanic fan.

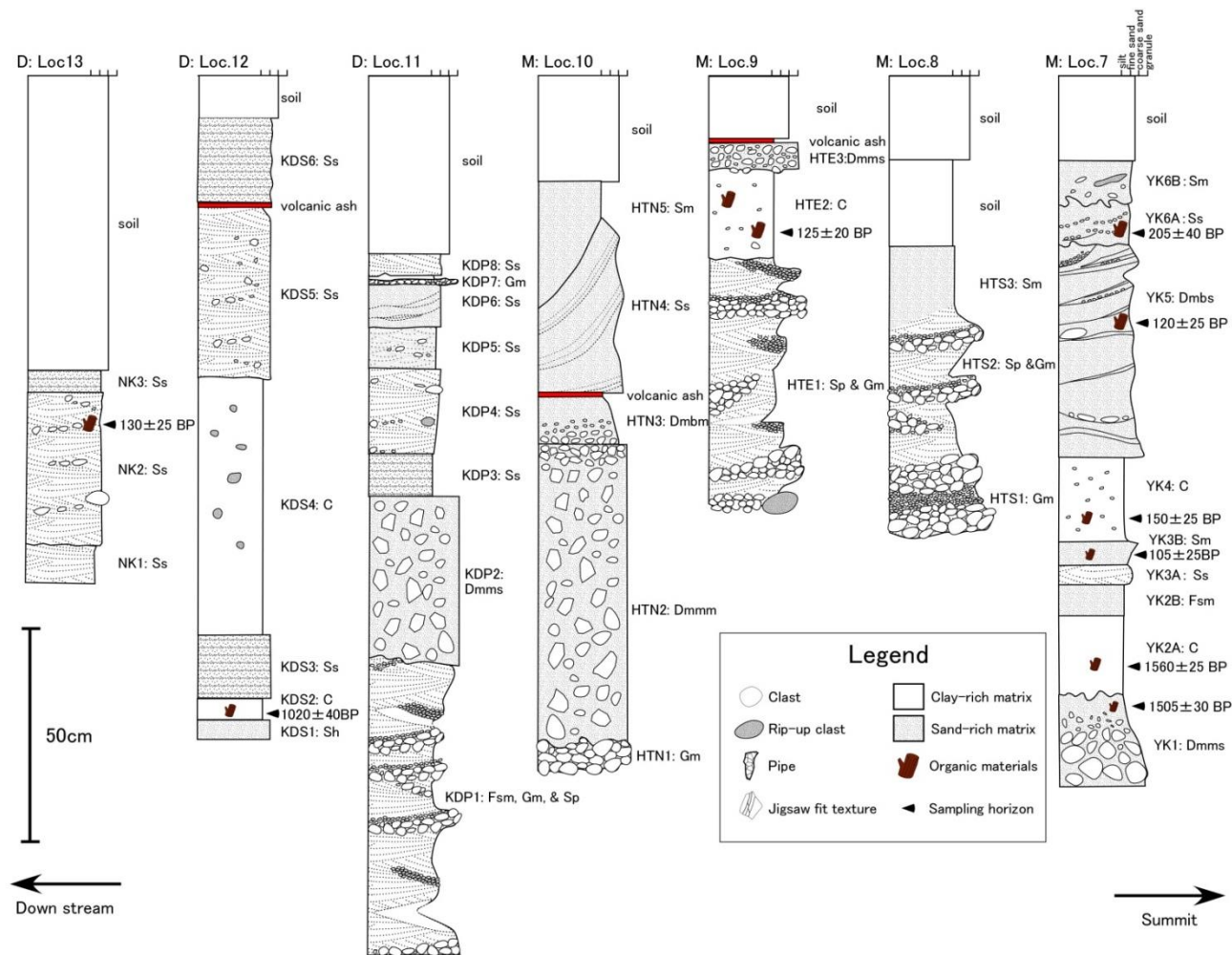


Fig. 2.7. Stratigraphic sections in the excavation sites. Locations are shown in Figs. 2.5 and 2.6. The Kisakata debris avalanche deposit (KDAD) is overlain by the volcanic fan deposits. The codes beside the sections correspond to unit names and sedimentary facies (see chapter 2.5). The codes beside the location number correspond to the area observed trenches classified: M: the medial volcanic fan; and D: the distal volcanic fan. Results of the ^{14}C dates on the right of the columns are fully described in Table 2.1.

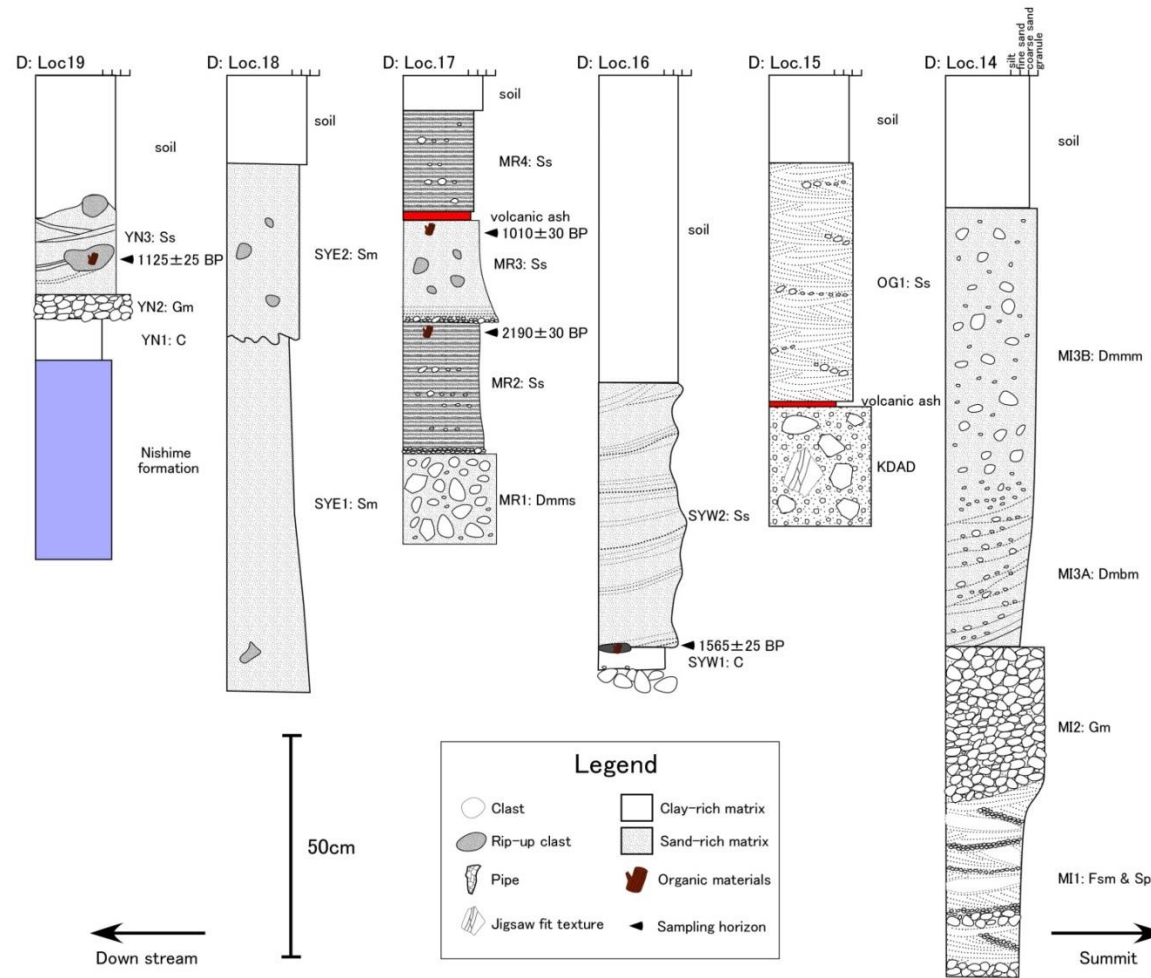


Fig. 2.7. (continued)



Fig. 2.8. Photographs of the volcanic fan deposits in the proximal volcanic fan. (A) Matrix-supported massive diamicton with muddy matrix (Dmmm). (B) Clasts-supported massive diamicton with sandy matrix (Dmcs). (C) Clast-supported massive diamicton with muddy matrix. (D) Matrix-supported bedded diamicton with muddy matrix (Dmbs).

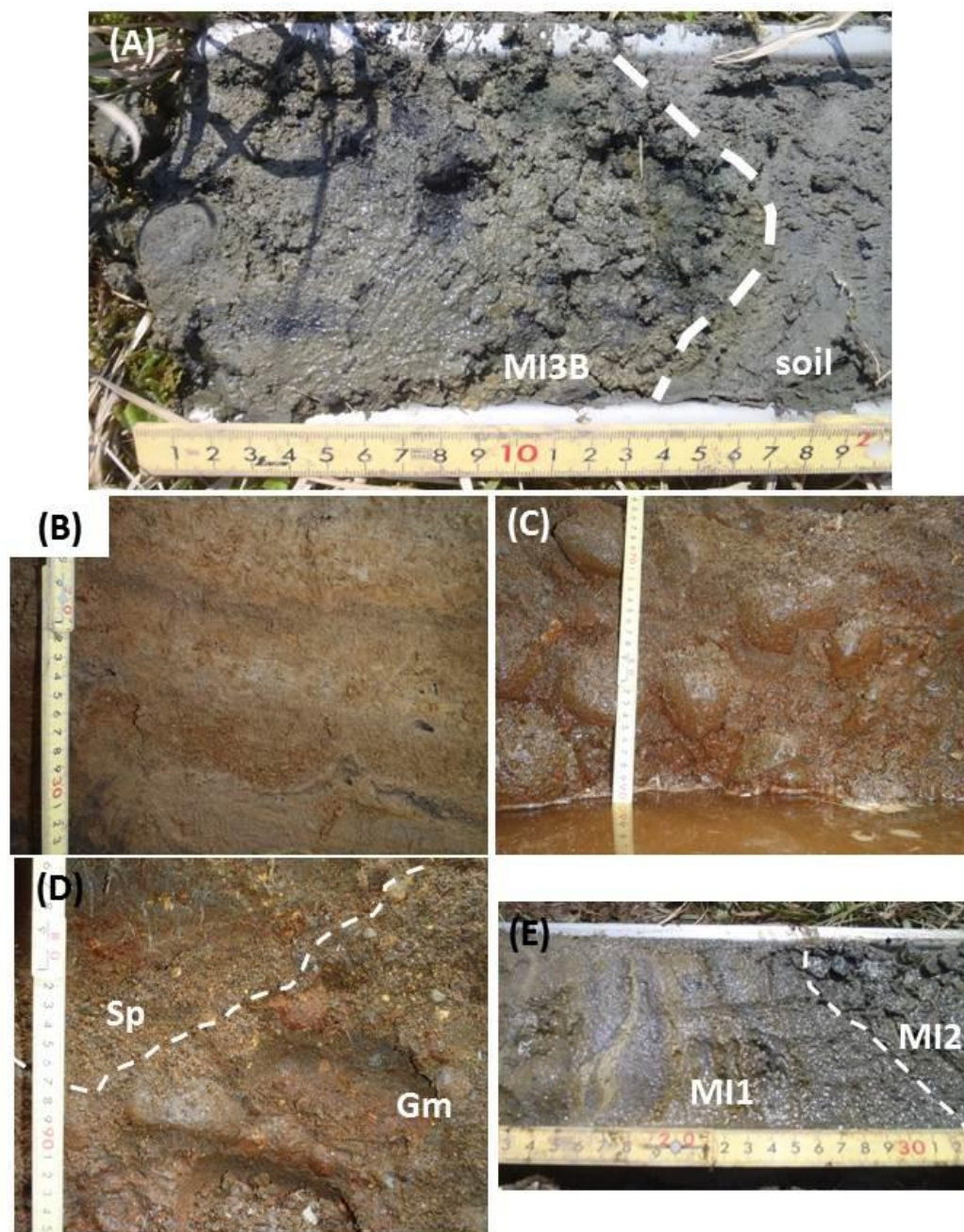


Fig. 2.9. Photographs of the volcanic fan deposits in the excavation sites in the medial and distal volcanic fans. (A) Matrix-supported massive diamicton with muddy matrix (Dmmm) observed in the core at Loc. 14 (MI3B; Fig. 2.7). (B) Matrix-supported bedded diamicton with sandy matrix (Dmbs) at Loc. 7 (YK5; Fig. 2.7). (C) Clast-supported weakly grading gravel (Gm) at Loc. 8 (HTS1; Fig. 2.7). The clasts are stained with a reddish coat, indicating oxidization/hydration of iron compound. (D) Alternated layers of Gm and Sp at Loc. 8 (HTS2; Fig. 2.7). The layers show high-angle stratification. (E) The contact between the facies Gm (MI2) and MI1 that is the alternation of Sp (grayish) and Fsm (whitish) in the core at Loc. 14 (Fig. 2.7).

The facies Dmm is subdivided into two subfacies, Dmmm (muddy) and Dmms (sandy), based on the grain-size and components of the matrix. The clasts in Dmmm range from clay to boulder, and medium sand is dominant in their matrix. Altered clasts are richer in Dmmm than Dmms. Clasts in Dmms range from fine sand to boulder, and coarse sand is the most dominant in the matrix.

Interpretation: The characteristics of this facies indicate debris flow deposition and the en masse sedimentation rather than the grain-by-grain sedimentation (Shultz, 1984; Smith and Lowe, 1991). The containment of large gravels suggests that the debris flow had high energy.

Facies Dmc: Clast-supported massive diamicton with sandy (Dmcs) or muddy (Dmcm) matrix

Description: Deposits of facies Dmc are 50 to 200 cm thick and characterized by clast-supported gravels (Fig. 2.8B and C; Minami et al., 2015). The deposits appear only in the proximal volcanic fan. The deposits are composed of particles with a broad range of size from fine to boulder up to 100 cm. The gravels are subrounded, ranges from pebble to boulder, and composed mainly of fresh andesite. The facies frequently contains gravels of altered volcanic rocks that show various colors from grayish blue to grayish white, indicating different degree of alteration. Minor muddy rip-up clasts are contained too. Preferred clast orientations are present. The deposits are massive, poorly sorted and lacking interstratification and clear grading, whereas coarse-tail normal grading from cobble to granule is rarely observed. Contacts with underlying deposit are clear and erosive.

The facies Dmc is subdivided into two subfacies, Dmcm (muddy; Fig. 2.8C) and Dmcs (sandy; Fig. 2.8B), based on the grain-size and components of matrix. The clasts in Dmmm range from clay to boulder, and medium sand is dominant in their matrix. Altered clasts are richer in Dmmm than Dmms. Clasts in Dmms range from fine sand to boulder, and coarse sand is the most dominant

in the matrix.

Interpretation: The characteristics of the facies indicate debris flow deposition. The characteristics imply the *en masse* sedimentation rather than grain-by-grain sedimentation (Shultz, 1984; Smith and Lowe, 1991). The containment of large gravels suggests that the debris flow had high energy.

Facies Dmb: Matrix-supported bedded diamicton with sandy (Dmbs) or muddy (Dmbm) matrix

Description: Deposits of facies Dmb consist of sand and gravel (Figs. 2.8D and 2.9B). The deposits are 20 - 450 cm thick in the proximal area (Minami et al., 2015) and 10 - 50 cm in the medial and distal volcanic fan. The deposits are characterized by features of diffuse beddings, poor sorting, and matrix supporting (Figs. 2.8D and 2.9B). Clasts are unaltered andesite mostly, but minor altered andesitic clasts with different degree of alteration are also contained. These clasts exhibit orientation in which the long-axes are parallel to the beddings. The deposits contain silt-coarse sand layers that show diffuse and horizontal beddings. Granule-pebble layers are contained too. Contacts of the layers are unclear, showing no evidence of hiatus or erosion. Sorting is better than that of facies Dmm, but poorer than facies Ss. Individual layers are 2-20 cm thick. The facies rarely exhibit unclear laminar or beddings that are parallel or cross-bedded in low-angle. Outsized gravels (up to 200 cm) are sparsely contained.

The facies Dmb is subdivided into two subfacies, Dmbm (muddy; Fig. 2.8D) and Dmbs (sandy; 2.9B) based on the grain-size and the components of the matrix. The matrix of Dmbm consists of blue grayish silt-fine sand, whereas that of Dmbs consists of yellowish brown sand.

Interpretation: The characteristics of matrix-supported, poorly sorted, and diffuse stratification of Dmb are the same with those of the hyperconcentrated flow deposit (Smith, 1986; Smith and Lowe, 1991), and clearly different from those of deposits formed by *en masse* or grain-by-grain depositions. The diffuse

stratification of alternation of finer-grained and coarser-grained layers, absence of the erosional boundary, clear grading in interbedded layers, or high-angle cross/parallel stratification imply that rapid deposition of sediment rather than grain segregation during grain-by-grain transportation. The deposits contain large boulders (up to 200 cm), indicating high energy of the flow.

Facies Gm: Clast-supported weakly grading gravel

Description: Deposits of facies Gm consist of gravels that are massive, upward fining, and sorted. The deposits form layers ranging from 2 to 35 cm thick (Fig. 2.9C). The deposits contain well-rounded andesitic gravels (granule to boulder) in close-framework structure. The clasts are often stained by a reddish coat. Each deposit shows fine-upward grading. Lenticular layer is common. The gravel layer is associated with multiple sand layers that show plane bedding or lamination (Facies Sp and Fsm: Figs. 2.9D and E). The boundaries between the Gm layer and the sand layers are conspicuous, indicating that they are old erosional surfaces.

Interpretation: Sedimentation in gravel bars is indicated by the gravel facies that is sorted and shows close-framework structure (Miall, 2010). The feature is different from the deposits produced by *en masse* emplacement.

Facies Sp: Bedded sand

Description: Deposits of facies Sp is 10 to 15 cm thick and characterized by well bedded, sorted, and medium to very fine-grained sand (Fig. 2.9E). Each bed of facies Sp shows a clear normal distribution grading.

Interpretation: The features of well bedding, sorting, and normal grading indicate deposition from a traction current. These features typically indicate environments of sand bars (Miall, 2010).

Facies Ss: Sand with parallel to low-angle cross-bedding

Description: Facies Ss is characterized by 10 to 60 cm thick sand layer that shows parallel to low-angle cross lamination (Figs. 2.10A and B). Sorting is better than those of Dmm or Dmb. Rounded andesitic gravels (<~10 cm in diameter) are rarely contained. These gravels are altered in different degrees, but unaltered andesitic gravels are most abundant. The sand consists of lithic fragments, scoria, and free crystals of rock-forming minerals such as plagioclase. Each bed shows normal distribution grading. The deposit overlies a massive mud (Facies C) layer with a clear erosional boundary commonly.

Interpretation: The features of sandy beds, sorting, and parallel/low-angle cross lamination/bedding, indicate grain-by-grain deposition from low-density flow (Smith and Lowe, 1991). The deposit commonly overlies a facies C deposit that was formed in a static environment. This relation between facies Ss and C implies episodic inflow that feeds sand into a static environment. The characteristics of the facies imply grain-by-grain deposition from overflowed and diluted stream flow (Smith and Lowe, 1991; Vallance, 2000). The streamflow was generated by transformation from other flow types of upstream lahar.

Facies Sm: Massive sand

Description: Facies Sm is characterized by 10-20 cm thick sand layers that are massive and poorly sorted. Grain size ranges from very fine to medium sand. The deposit contains abundant pebble-sized exotic clasts originated from consolidated, well-sorted Neogene sandstone consisting of fine-medium sand. The facies contains abundant plant fragments and root trace. The facies Sm grades downward into well-structured sand.

Interpretation: Massive, poorly sorted facies and containment of sandstone clasts suggest that facies Sm results from rapid deposition from sediment gravity flow or post-depositional modification of sandy facies such as Sp and Ss (Smith, 1986).

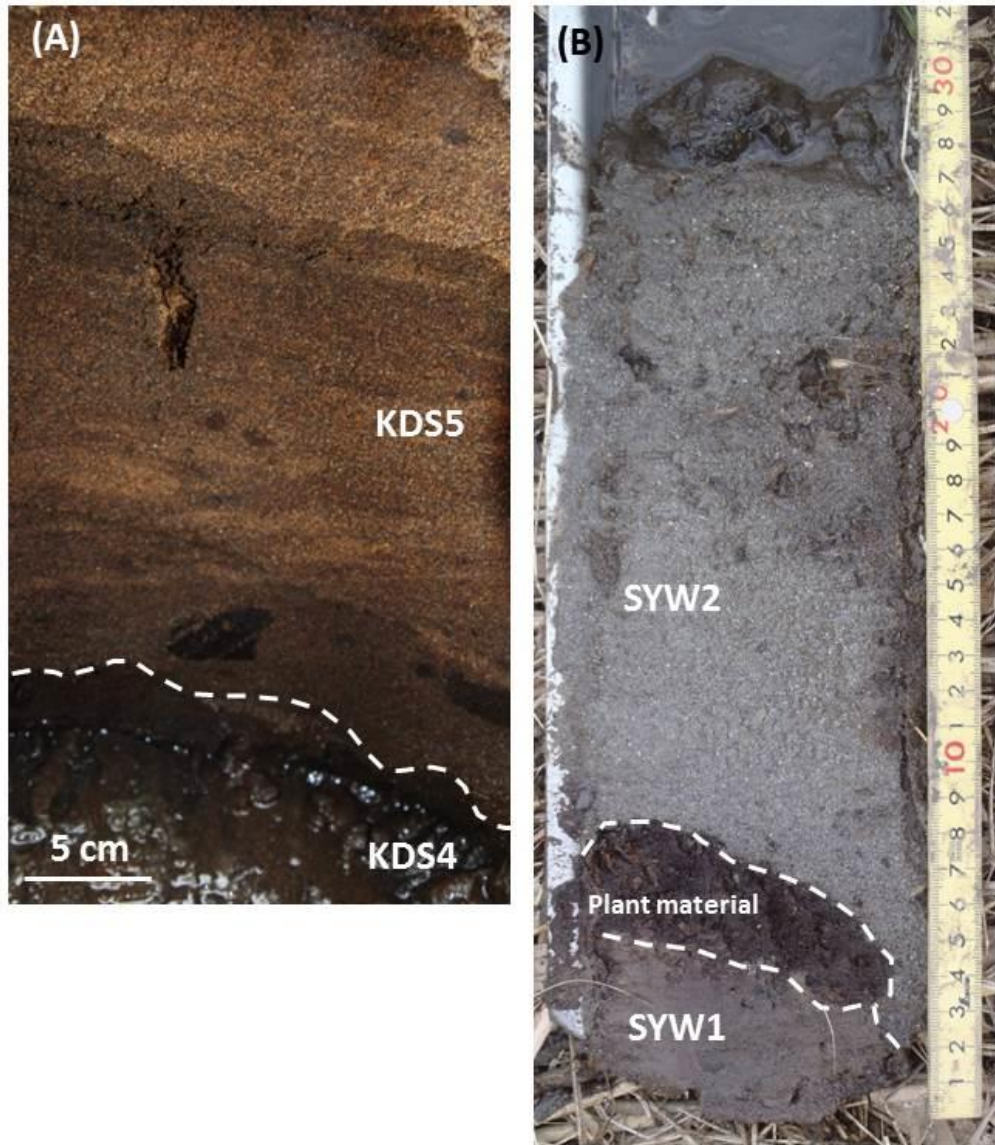


Fig. 2.10 Photographs of the facies Ss overlying the facies C at Locs.12 (A) and 16 (B).

Facies Fsm: Fine massive sand

Description: Facies Fsm represents layers of massive and well-sorted very fine sand or silt. The layers are less than 15 cm thick, grade downward into well-bedded sand (Facies Sp), and have lenticular dimensions intercalating with facies Gm and Sp (Fig. 2.9E). Plant fragments and root traces are rare.

Interpretation: The characteristic of facies (massive and well-sorting), lenticular dimension, and intercalation with stratified gravels and sand imply that facies Fsm represents a floodplain facies (Miall, 2006, 2010).

Facies C: Carbonaceous mud

Description: Facies C is characterized by massive and carbonaceous silt or mud layers. Layers of the facies are ~60 cm thick and contain abundant sand patches and plant fragments including *oryza sativa* seeds (Fig. 2.10B).

Interpretation: Massive and carbonaceous silt to mud typically associated with, floodplain environments (Miall, 2010).

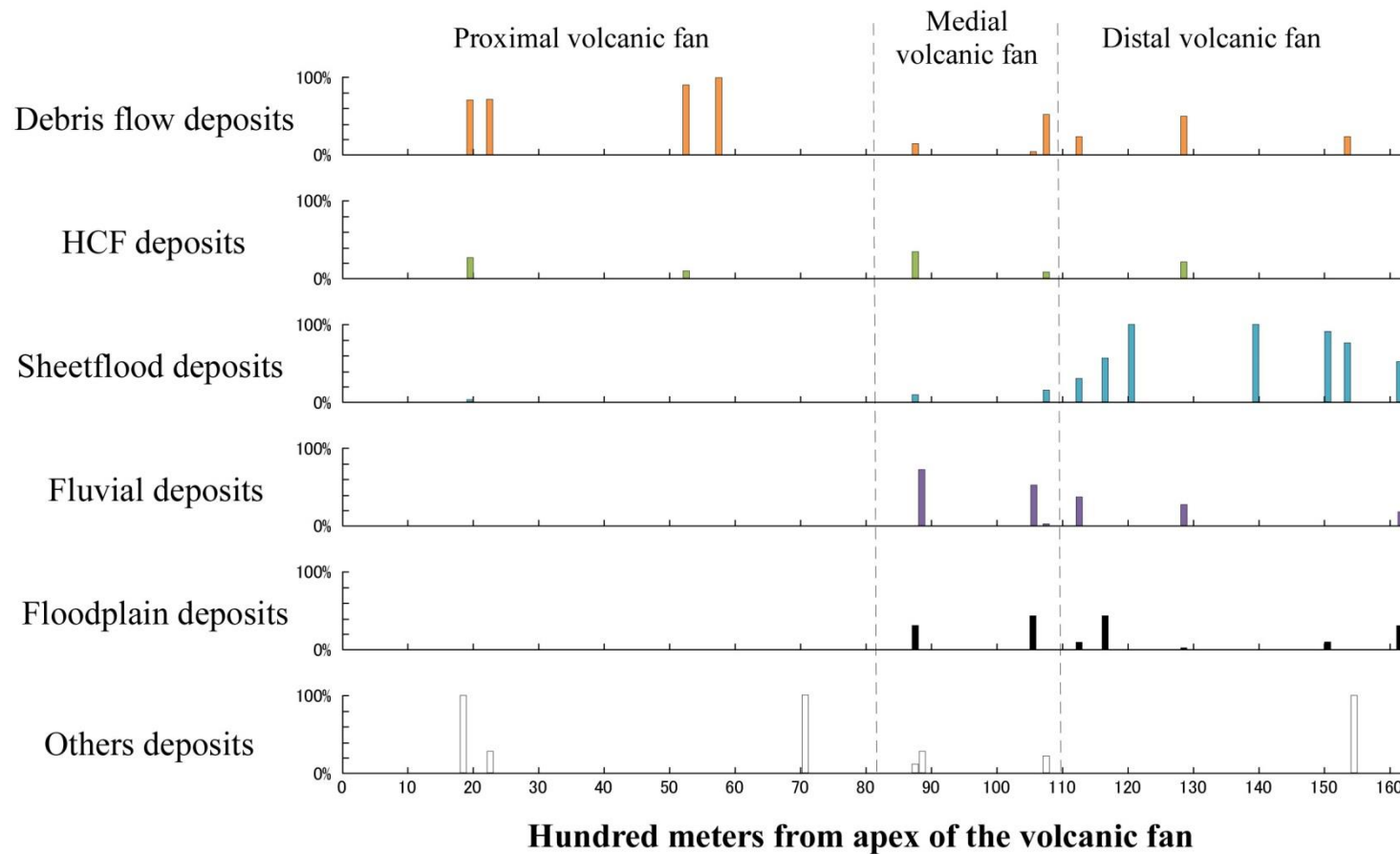


Fig. 2.11. Diagram illustrating relative abundance of the sedimentary facies showing the variation with the distance from the apex of the volcanic fan. Open bars: basement rocks (Sasaoka Formation, Nishime formation, Shirayukigawa pyroclastic density current deposit SPDCD, and the Kusakata debris avalanche deposit KDAD); Orange bars: debris flow deposits (Dmmm, Dmms, Dcmm, and Dcms); green: hyperconcentrated flow deposits (Dmbm and Dmbs); blue bars: facies Sm; purple bars: fluvial deposits (Gm and Sp); sky-blue bars: sheetflood deposits (Ss); and black bars: mud (facies Fsm and C).

2.6. Facies change from proximal to distal areas

2.6.1. Proximal volcanic fan

Facies association in proximal represents a proximal volcanic fan environment composed mainly of a series of debris flow and hyperconcentrated flow deposits overlying the KDA, as described in our previous study (Fig. 2.6: Minami et al., 2015). In the upper area of the proximal volcanic fan (Loc.2 and 3; Figs. 2.6 and 2.11), debris flow facies is dominant and accounts for ~70 %, and hyperconcentrated facies for 20 %. In the lower area of the proximal volcanic fan (loc. 4 and 6; Figs. 2.6 and 2.11), the deposits are composed mostly of debris flow facies (90-100 %: Fig. 2.11). Paleosol layer is not included with the pile of debris flow and hyperconcentrated flow deposits, indicating no sign of hiatus. The basement Neogene sediments and KDA are exposed at the river-bed of Shirayukigawa and the southern side of Nikaho hill (Loc. 1 and 5; Figs. 2.6 and 2.11), where overlying sediments may be removed by river wash and small-scale landslides.

2.6.2. Medial volcanic fan

Facies association changes in the medial volcanic fan with the gradients of fan surface or the distance from the volcanic edifice. The medial volcanic fan (Loc. 7 – 10: Fig. 2.7 and 2.11) is dominated by fluvial facies (Gm, Sp, and Fsm) and debris/hyperconcentrated flow facies (Dmmm, Dmms, Dmcm, Dmcs, Dmbm, and Dmbs). Coexistence of the fluvial facies and debris flow and hyperconcentrated flow deposits is not common in a location (only at Loc. 7). The facies observed in Loc. 7 - 10 indicate that spatial distribution of debris/hyperconcentrated flow facies and fluvial facies are mingled in the area. Fluvial facies accounts for 70 % at Loc. 8 and 9, whereas the debris/hyperconcentrated flow facies account for 50 % in Loc. 7 and 10 (Fig. 2.11). Hiatuses among rapid depositional events are evident from the presence of facies C at Loc. 7 and 9 (Fig. 2.7). The hiatuses are not recognized in the proximal area.

2.6.3. Distal volcanic fan

In the distal volcanic fan (Loc. 11-19; Fig. 2.7), facies Ss is dominant except for three locations (Loc. 11, 14 and 18). Facies Ss accounts for 60 to 100 % at other locations. At Loc. 18, predominant facies is Sm, which probably pedogenetic sand derived from other sandy facies such as Sp and Ss (Fig. 2.11). Debris flow and fluvial facies are locally distributed (Loc. 11, 14 and 16; Fig. 2.7). Floodplain facies (Fsm and C) are also major components in the distal volcanic fan. Floodplain facies distribute at most locations (Loc. 11, 12, 14, 17, and 19; Figs. 2.7 and 2.11) and account for ~40%. The presence of the facies Fsm and C interbedded with the facies Ss represents development of a static environment with occasional sand inflows into the distal volcanic fan. In northeast area of the distal volcanic fan, where near the Yokone district, basement rocks and KDAD are distributed (Loc. 15 and 19; Fig. 2.7).

2.7. Minerals in the lahar deposits

Minerals identified in the lahar deposits are listed in Table 2.1. The XRD measurement elucidated that plagioclase occurs in all units, except ND8. Clay-minerals, which are pyrophyllite, 7-Å kaolin group mineral (any of kaolinite, nacrite, or dickite), chlorite, and smectite, are also common. Mineral assemblages in lahar deposits are classified broadly into two groups: one group shows intensity X-ray peaks of plagioclase with minor X-ray peaks of clay-minerals (ND9-16), and the other shows intensity X-ray peaks of clay-minerals (ND1-8). The X-ray peaks of gypsum, pyrophyllite, 7-Å kaolin group mineral, and smectite occur in: ND1, 2, and 8; ND4, 5, 6, and 8; ND2, 3, 4, 6, and 8; and ND2, 3, 5, and 8, respectively. ND8 shows intense X-ray peaks of cristobalite, pyrophyllite, 7-Å kaolin group mineral, smectite, and pyrite.

Table 2.1 Identified mineral assemblages (using XRD) from the lahar deposits. Abbreviations are: Qtz: quartz; Cri: cristobalite Pl: plagioclase; Smect: smectite; Kao: kaolin-group mineral; Prl: pyrophyllite; Chl: chlorite; Alu: alunite; Gyp: gypsum; and Pyr: pyrite. Symbols indicate X-ray peak intensities: ***: intense; **: moderate; *: weak; -: faint.

Layer	Qtz	Cri	Pl	Smect	Kao	Prl	Chr	Alu	Gyp	Pyr
ND1	**	-	***	**	**		**	*	-	
ND2	*		***	**	*		-	**		
ND3	*		***	***	***		*	*		
ND4	**	-	***	*	**		**			
ND5	**		***	**	***					
ND6	**		***	*	***					
ND7	*		***	-	*			-		
ND8	*	***		***	***	*				**
ND9	-		***	*						
ND10	**		***	*	*					
ND11	**		***	-	**					
ND12	*		***		*					
ND13	**		***	-	*		*			
ND14	*		***		*					
ND15	*		***		*					
ND16	*		***		**					

2.8. Carbon 14 dating

Radiocarbon ages range from 2190 ± 30 to 150 ± 25 yrBP, accordingly from 361–178 calBC to present in calendar age (Table 2.2). Each calendar age falls into one of four ranges; 360-180 cal BC (Beta-MR2), 420-640 cal AD (JAT-YK1, JAT-YK2A, and JAT-SYW1), 869-1150 cal AD (Beta-KDS2, Beta-MR3, and JAT-YN3), and 1670 cal AD to present (JAT-YK3B, JAT-YK4, JAT-YK5, JAT-YK6, JAT-HTE2, and JAT-NK2).

The oldest age (2190 ± 30 yrBP) was obtained from an organic sediment sampled from sandy stream flow deposit at Loc. 16 (Beta-MR2). The calculated ages ranging from 420 to 640 cal AD were obtained from the charcoals sampled from the debris flow deposit (YK1: 1505 ± 30 yrBP) and the flood plain deposit (YK2A: 1560 ± 25). The age of a plant fragments sampled from floodplain deposit also fall into the same range (SYW1: 1565 ± 25 yrBP). The calculated ages ranging from 780 to 1150 cal AD were obtained from plant fragments sampled from the floodplain deposit (KDS2: 1020 ± 40 yrBP) and the dilute stream flow deposit (YN3: 1125 ± 25), and charcoal sampled from the dilute stream flow deposit (MR3: 1010 ± 30 yrBP). The calculated age ranging from 1670 cal AD to present were obtained from plant fragments sampled from the hyperconcentrated flow deposit (YK5: 120 ± 25 yrBP), the dilute stream flow deposit (YK6: 205 ± 40 yrBP) and the floodplain deposits (YK4: 150 ± 25 yrBP; and HTE2: 125 ± 20 yrBP) and the charcoal sampled from the dilute stream flow deposit (NK2: 130 ± 25). The age of a plant fragments sampled from YK3B (facies Sm) also falls into this range (105 ± 25 yrBP).

The organic pieces enclosed in the debris/hyperconcentrated flow deposits and the streamflow deposits are interpreted as the organic pieces were trapped at the time of deposits emplaced. Accordingly, the radiocarbon ages of these organic samples represent the approximate time of the emplacement. The organic pieces sampled from floodplain deposits which are directly overlain by debris/hyperconcentrated flow deposit and dilute stream flow deposit also

Table 2.2 Results of ^{14}C dating of lahar deposits and intercalated paleosoils.

Unit name	Facies code	Sample ID ¹	Sample type ²	Preparation ³	$\delta^{13}\text{C}(\text{‰})$	^{14}C age (yrBP) ⁴	Calendar age (calAD or calBC)
YK1	Dmms	JAT-YK1	C	AAA	-24.96	1505±30	431 - 635 (95.4)
YK2A	C	JAT-YK2A	C	AAA	-24.17	1560±25	424 - 555 (95.4)
YK3B	Sm	JAT-YK3B	P	AAA	-28.00	105±25	1682 - 1735 (27.5) 1806 - 1930 (67.9)
YK4	C	JAT-YK4	P	AAA	-26.65	150±25	1667 - 1707 (16.3) 1719 - 1783 (33.9) 1796 - 1826 (11.3) 1832 - 1885 (16.4) 1913 - 1950 (17.5)
YK5	Dmbs	JAT-YK5	P	AAA	-28.49	120±25	1680 - 1764 (31.4) 1801 - 1939 (64.0)
YK6	Ss	JAT-YK6	P	AAA	-26.63	205±40	1640 - 1698 (23.3) 1725 - 1815 (47.5) 1835 - 1878 (3.8) 1916 - present (17.9)
HTE2	C	JAT-HTE2	C	AAA	-26.95	125±20	1681 - 1739 (27.6) 1744 - 1763 (3.4) 1802 - 1894 (50.0) 1906 - 1939 (14.4)
KDS2	C	Beta-KDS2	P	AAA	-24.9	1020±40	900 - 1152 (95.5)
NK2	Ss	JAT-NK2	P	AAA	-29.92	130±25	1677 - 1765 (35.1) 1773 - 1777 (0.8) 1800 - 1893 (44.5) 1907 - 1940 (15.0)
SYW1	C	JAT-SYW1	P	AAA	-27.03	1565±25	421 - 551 (95.4)
MR2	Ss	Beta-MR2	OR	AW	-23.2	2190±30	361 - 178 (95.4) cal BC
MR3	Ss	Beta-MR3	C	AAA	-26.0	1010±30	973 - 1049 (82.4) 1085 - 1125 (10.4) 1137 - 1150 (2.6)
YN3	Ss	JAT-YN1	P	AAA	-23.78	1125±25	779 - 789 (1.3) 869 - 990 (94.1)

1: Sample IDs include the abbreviations of laboratories and the geological units. The sample IDs with JAT were analyzed at the Japan Nuclear Cycle Development Institute Tono Geoscience Center, and those with Beta at the Beta Analytical Inc. For the samples analyzed at the Japan Nuclear Cycle Development Institute Tono Geoscience Center, the isotopic ratios of $^{14}\text{C}/^{12}\text{C}$ and $^{14}\text{C}/^{13}\text{C}$ were measured with JAEA-AMSTONO (15SDH-2; National Electrostatics Corp.) installed at Japan Nuclear Cycle Development Institute Tono Geoscience Center (Xu et al., 2000).

2: Sample types are abbreviated as; C: charcoal; P: plant fragments; and OR: organic sediment.

3: Preparation methods are abbreviated as AAA: acid/alkali/acid and AW: acid washed.

4: All errors are 1-sigma of standard deviation.

represent the approximate time of the emplacement of the overlaying deposit.

2.9. Discussion

2.9.1. Depositional processes of fan deposits

The fan deposits are composed mainly of epiclastics. The sedimentary facies are classified broadly into two types regarding transportation and depositional mechanisms. One was formed by the rapid transportation-deposition from debris flow and hyperconcentrated flow (Dmmm, Dmms, Dmbm, and Dmbs), and the other formed by the gentle transportation-deposition from traction current or sluggish stream (Gm, Ss, Sp, Fsm, C).

The components of the volcanic fan deposits are derived from Chokai volcano. The dominant rock type of the clasts is andesite that occurs only on the cone of Chokai volcano along the Shirayukigawa river system. In fact, the debris/hyperconcentrated flow deposits are distributed on the skirt of the volcanic cone of Chokai. As the rapid transportation-deposition from debris flows and hyperconcentrated flows occurred on the volcanic cone, the flows can be regarded as lahars (Smith and Fritz, 1989; Smith and Lowe, 1991; Vallance and Iverson, 2015), rather than normal fluvial processes. The facies Ss indicates deposition from diluted stream flow. The intercalation with the facies C and Fsm indicates episodic inflows of sand into a static environment, which were caused by broad sheetfloods overflowed from the paleochannel. The original flows in the channel were debris/hyperconcentrated flows in upstream, as upstream debris/hyperconcentrated flows can transform into diluted stream flows in downstream (Smith and Lowe, 1991; Vallance, 2000). Because the inflow is the continuous phenomena to the upstream debris/hyperconcentrated flow, we regard this inflow as a part of lahar. We here use the term “lahar deposits” for the all the deposits that originate from debris flow, hyperconcentrated flow, and sheetflood in the volcanic fan.

2.9.2. Relationship between geomorphology and distribution of lahar deposit

The dominant facies in a location changes with distance from the volcanic edifice. The geomorphological features are also related to the distance. Therefore, dominant facies relates to the geomorphology on the volcanic fan surface. The debris flow facies are dominant in the proximal volcanic fan, which geomorphology is characterized by high surface gradient and by development of debris flow lobes (Minami et al., 2015).

With the distance from the volcanic edifice, the surface gradient decreases to 1-2° and the debris flow lobes become smaller and obscure. In the medial volcanic fan, the dominant facies at a location is either of debris flow or hyperconcentrated flow. The debris flow deposits first emplaced on this area that has a gentle surface (> 2-3°). The depositional condition of surface gradient is consistent with Rodolfo (1989) and Vallance and Scott (1997). Then, the debris flow deposit was partly erased by the activities of fluvial system. The mingled distribution of debris flow facies and fluvial facies was caused by the overprint of the fluvial facies on the debris flow facies. The diffusiveness of debris flow lobes and the localization of debris flow deposits are attributed to the incompleteness of this erasure of debris flow deposits by fluvial development. The fluvial succession at each location shows a quite unstable depositional environment, inferred from thin layers (<30 cm) of various facies such as gravel bar, sand bar, and floodplain (HTS2, HTE1, KDP1, and MI1; Fig. 8D and E). This instability of the system may be attributed to rejuvenation by lahar inflow into the fluvial system to disturb the hydrology (Pierson and Major, 2014). This inflow process is preserved in some successions (Loc. 10 and 11, Fig. 7), indicating a debris flow deposit (HTN2 at Loc.10 and KDP2 at Loc. 11) overlay the fluvial deposit (HTN1 at Loc. 10 and KDP1 at Loc. 11), and then a sheetflood deposit covered the debris flow deposit (HTN4 at Loc. 10 and KDP3 at Loc. 11).

The distal volcanic fan is composed mostly of sheetflood and floodplain deposits. Interbedding of the sheetflood sand (Ss) with the floodplain deposits

(Fsm and C) implies sporadic inflows into the floodplain where the channel is static. The well-developed pedogenic sediments without any sign of erosion indicate the steadiness of the environment. The smooth and near-flat surface may be a depositional surface of these sheetflood deposits. Thickness of this distal succession decreases northward, and basement rocks (KDA and the Neogene sediments) appear at very shallow levels near the end of the plain (Loc. 15 and 19; Fig. 7). Locally distributed conglomeratic deposits are attributed to some large-scale debris flows that can flow down even on very flat surface to a large extent (Lopez et al., 2003; Pierson, 1995).

The density of hummocky hills increases outward. Hummocky hills are distributed in the medial and the distal volcanic fans, as well as in the hilly area. The density of hummocky hills is higher in the hilly area and the Kamigo-Konoura hill than those in the volcanic fans. The density is higher in the distal volcanic fan than that in the medial volcanic fan. These spatial variations of the density of hummocky hills may result from a burying of the original hummocky hills by aggradation of the volcanic fan deposits. On the other hand, in the hilly area (and the Kamigo-Konoura hill), the hummocky hills have preserved their original morphologies which were free from the burying, indicated by the density.

2.9.3. Temporal component—change of Lahar Deposits

Mineral assemblages in lahar deposits are classified broadly into two groups: one group shows intensity X-ray peaks of plagioclase with minor X-ray peaks of clay-minerals, and the other shows intensity X-ray peaks of clay-minerals (Table 2.1). The lower 8 units (ND1-8) contain abundant clay-minerals and the upper 8 units (ND9-16) contain abundant plagioclase and minor clay-minerals. The mineral assemblages of clay-minerals are typical of hydrothermal alteration zones in magmatic-hydrothermal systems under subduction zone volcanoes (Rye et al., 1992; Hedenquist and Lowenstern, 1994). The mineral assemblages, therefore, indicate that the clay-minerals were derived from a

subvolcanic hydrothermal system. The compositional change between ND8 and ND9, therefore, indicates that change of source materials from hydrothermally altered materials to unaltered volcanic rocks.

Sub-volcanic hydrothermal system beneath Chokai volcano can be considered as a source of the hydrothermally altered materials in the lahar deposits, because of only Chokai volcano has sub-volcanic hydrothermal system in the area of catchment topography of Shirayukigawa system. To explain component-change between ND8 and ND9, we can assume two types of deriving mechanisms. 1) Hydrothermally altered materials were derived by landslide from hydrothermally altered zone exposed by edifice-collapse at 2.5ka. The component-change suggests that altered materials decreased according to hydrothermally altered zone were buried. 2) Hydrothermally altered materials were derived by hydrothermal eruptions and the component-change reflecting that the eruptions changed from hydrothermal to magmatic. The later is corresponding the eruption history organized based on a pile of tephra layers on the volcanic flank (Ohba et al., 2012).

2.9.4. Correlation between lahar events and eruptive history

Here, we correlated the lahar events and the eruptive history from the ^{14}C ages and the previous reports on eruptive history (Ueki and Hori, 2001; Hayashi, 2001; Hayashi et al., 2012, 2013). The foundation of the volcanic fan was formed by the emplacement of the debris flow avalanche deposit of KDA in BC 466 (Mitsutani, 2001; Ohzawa et al., 1982). The oldest ^{14}C geochronological date (2190 ± 30 yrBP, or 421–551 cal BC, Table 1) in this study is obtained from an organic sediment (Beta-MR2) sampled from a sandy sheetflood deposit (MR2) at Loc. 16. This sheetflood deposit directly overlies a sandy debris flow deposit (MR1: Fig. 7 Loc. 17). From similarity in components, these sandy deposits (MR1 and MR2) can be correlated with some of the sandy debris flow deposits in

the upstream (Fig. 6). At Loc. 4, these sandy debris flow deposits consist of eight units (ND 9 - 16), overlying another pile of eight units of muddy post-collapse debris flow deposits (ND 1 - 8) (Minami et al., 2015). Because the age of MR2 is close to that of KDA, the series of muddy lahars (ND 1 - 8) were formed in a short period just after the collapse at 2.5 ka.

Very similar ages between the early 5th and the early 7th centuries were obtained from a debris flow deposit (YK1: 431-635 cal AD with a 95.4% reliability; Table 1) and two floodplain deposits (YK2A: 424 - 555 cal AD, 95.4%; SYW1: 421-551 cal AD, 95.4%; Table 1). As SYW1 is directly overlain by sheetflood deposit (SYW2), the lahar emplaced as sheetflood deposit during this period. The similarity of the ages implies a single lahar event.

The calculated ages between the late 8th and middle 12th centuries AD were obtained from the samples from the sheetflood deposit (YN3 and MR3) and the floodplain deposit (KDS2)(Table 1). As KDS2 is directly overlain by sheetflood deposit (KDS3), the date is the approximate age of the sheetflood (KDS3). The similarity of the dated ages implies that YN3, MR3, and KDS3 are the identical unit from a single lahar event. The range of the dating includes the ages of two witnessed eruptions in 871 and 939 (Ueki and Hori, 2001). An old document (Nihon Sandai Jitsuroku) reported that one of these eruptions, the 871 eruption, accompanied muddy slurry from the volcano. The muddy slurry killed river fishes and dammed the river. Although there are no descriptions about floods, the record may implies lahar occurrence. Accordingly, the dated unit is likely correlated with the lahar associated with the eruption in 871 AD.

The calculated ages younger than the late seventieth century from a hyperconcentrated flow deposit (YK5), sheetflood deposits (YK6 and NK2), floodplain deposits (YK4 and HTE2), and a unit YK3B (facies Sm). The deposits of YK4 and HTE2 are directly overlain by a hyperconcentrated flow deposit (YK5) and a debris flow deposit (HTE3), respectively. Therefore, the ages of underlying layers are the approximate dates of the hyperconcentrated flow (YK5)

and the debris flow (HTE3). Eight eruptions have been documented since the late seventieth century; 1659-1663, 1740-1747, 1792, 1800-1804, 1821, 1834, 1847, and 1974 (Ui and Shibahashi, 1975; Ueki and Hori, 2001). The occurrence of lahar that reached the distal volcanic fan was only documented for the 1801 eruption that is the climax of the activity between 1800 and 1804 (Hayashi et al., 2013; Hayashi and Minami, in printing). Therefore, the 1801 lahar is correlated with the lahar deposits of YK5, YK6, and HTE3.

As a result, at least lahars occurred four times to reach the distal volcanic fan. They occurred in the 5th – 6th century BC, the 5th – 7th century AD, 8th – 12th century AD, and 1801 AD. Therefore, such far-reaching lahars have occurred at least every 600 years. More lahars emplaced in the proximal volcanic fan, but many of them at least lower eight units (ND1-8) occurred just after the sector collapse at 2.5 ka.

2.10. Conclusion

The geomorphology of the volcanic fan varies with dominant facies of lahar deposits. The distal volcanic fan is characterized by steep gradients ($> 2^\circ$) and by development of lobes and is composed mainly of debris flow deposits. The medial volcanic fan is characterized by moderate gradients ($1^\circ - 2^\circ$) and by diffusive debris lobes and comprises both debris flow and fluvial deposits. The distal volcanic fan has a near-flat even plain ($< 1^\circ$), and is composed mainly of sheetflood deposits and floodplain deposits. At least 16 units of lahars settled in the proximal volcanic fan, and at least eight of them occurred just after the sector-collapse in 2.5 ka. The stratigraphic variation in the matrix component is consistent with the change in matrix mineral assemblage, possibly reflecting changes in the source materials from Chokai volcano. Some lahars reached the distal volcanic fan as sheetfloods. Such large-scale lahars occurred at least four times, the 5th – 6th century BC, the 5th – 7th century AD, 8th – 12th century AD, and 1801 AD.

CHAPTER III

MINERALOGICAL STUDY ON VOLCANIC ASH OF THE ERUPTION ON 27TH SEPTEMBER 2014 AT ONTAKE VOLCANO, CENTRAL JAPAN: CORRELATION WITH PORPHYRY COPPER SYSTEMS

3.1. Introduction

The zonation of alteration minerals produced in a hydrothermal system reflects spatial variations in hydrothermal processes and hydrothermal fluid chemistry (e.g. Meyer and Hemley, 1967; Rose and Burt, 1979; Reed, 1997). The relation between the distribution of hydrothermal fluid and consequent mineralogical zonation has been intensively studied through geological studies on geothermal fields as well as ore deposits. Some of the fields are considered to be the interior of ancient stratovolcanoes, and their structural models have been well established (e.g. Meyer and Hemley, 1967; Sillitoe and Gappe, 1984; Sillitoe, 2000, 2010; Hedenquist et al., 2000). Although the depths of hydrothermal systems are largely inaccessible under active volcanoes, we are able to obtain minerals precipitated at the depths when a hydrothermal eruption supplies them from the depths to the earth surface (Hedenquist and Henley, 1985).

Volcanic ash from the eruption at Ontake volcano on the 27th September 2014 consists abundantly of hydrothermally altered minerals (Miyagi et al., 2014), indicating the eruption was a hydrothermal eruption. The minerals were derived from the sub-volcanic hydrothermal system under the volcano, and therefore, the properties of hydrothermal alteration such as temperature, acidity, and locus can be estimated from the mineralogy of the volcanic ash. This study aims to estimate the chemical conditions and locus of the source fluid by correlating the mineralogy of the volcanic ash to proposed models of mineral zonation in well-studied ancient hydrothermal systems beneath eroded old volcanoes. The

estimation on the locus will be compared with previous geophysical estimations (Kato et al., 2015; Maeda et al., 2015).

3.2. Geological setting of Ontake volcano

Ontake volcano (3,067 MASL) located in central Japan, is a stratovolcano consisting of basalt, andesite, and dacite. The basement of Ontake volcano is largely composed of Jurassic to Paleogene rhyolite to rhyodacite and marine sediments (Yamada and Kobayashi, 1988; Takeuchi et al., 1998). Volcanic activity at Ontake volcano commenced 200 - 300 ka with effusion of basaltic to andesitic lava flows with minor dacite to form the ancestral volcanic edifice (Yamada and Kobayashi, 1988). The younger activity that formed the current edifice commenced at 80 ka. The activity is subdivided into two stages: the early explosive stage that produced rhyolitic to dacitic pyroclasts and the later lava stage. The lava is composed of andesite containing phenocrysts of plagioclase, orthopyroxene, clinopyroxene, and magnetite. The summit area at Kengamine is composed of andesite lava (Yamada and Kobayashi, 1988).

Phreatic (or hydrothermal) eruptions frequently occur at Ontake volcano. Before the 2014 eruption, at least three phreatic eruptions were documented in 1979, 1991, and 2007 (Oikawa et al., 2014). Oikawa et al. (2014) suggested that the frequency of phreatic eruptions of Ontake volcano is at least once in a few hundred years. Surface hydrothermal manifestations have been continuously observed on the southwestern flank of Kengamine cone for last 250 years (Oikawa, 2008). Hydrothermally altered rocks had been exposed on the southwestern flank of Kengamine before the 2014 eruption.

3.3. The 2014 eruption

The 2014 eruption took place on 27th September on the southwestern flank of Kengamine. The eruption ejected approximately a million tons of volcanic ash, similar to the volume of the 1979 eruption (Takarada et al., 2014),

and the Volcanic Explosivity Index (VEI) of the 2014 eruption was two (Earthquake Research Institute at the University of Tokyo, 2014; Japan Meteorological Agency, 2014). The volcanic ash was distributed in the summit area and on the eastern flank of the volcano (Fig. 3.1; Nakano et al., 2014; Takarada et al., 2014). Miyagi et al. (2014) reported that the volcanic ash consists exclusively of hydrothermally altered minerals with minor primary igneous

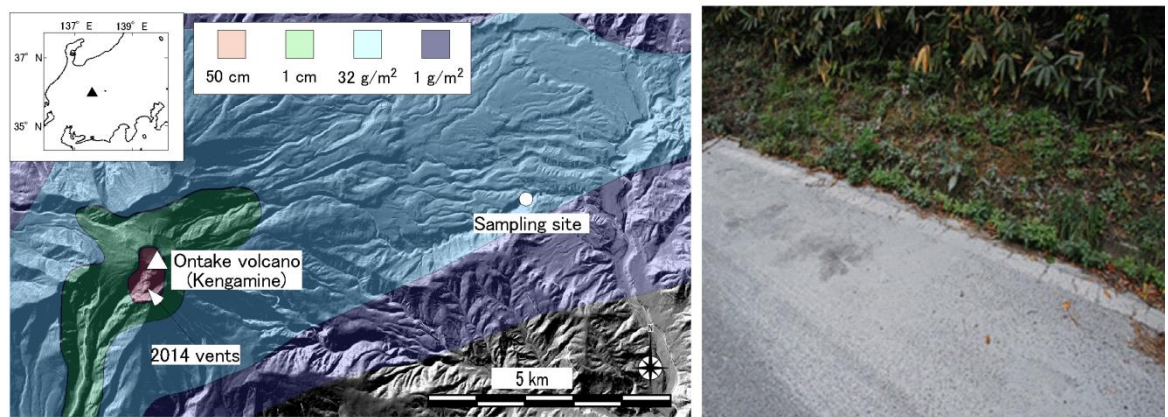


Figure 3.1. Location of sampling site (left) and volcanic ash from the eruption (right). Volcanic ash was sampled along the road. The samples were collected from clean, flat, and hard surface of the road and also from clean leaves. The volcanic ash distribution is drawn based on Takarada et al. (2014). The topographic relief map is created with Kasimir3D (Sugimoto, 2012) from the 10m-mesh DEM data provided by the Geospatial Information Authority of Japan.

particles. Some geophysical studies have reported analyses on seismicity linked to the eruption, investigating pre- and post- eruptive processes (e.g. Kato et al., 2015; Maeda et al., 2015; Ogiso et al., 2015).

3.4. Sampling and Methods

The volcanic ash from the 27th September 2014 eruption was sampled along a road 8 km northeast of the vent (Fig. 3.1). Particles were separated into three fractions: coarse ($>125 \mu\text{m}$), medium ($125 - 70 \mu\text{m}$), and fine ($<70 \mu\text{m}$)

fractions. The samples were analyzed with X-ray diffractometer (XRD) and SEM-EDS. Bulk ash samples were also analyzed by XRD.

Minerals were identified with the XRD (Multiflex; Rigaku Corp.) installed at Akita University. Measurements were carried out at a rate of 1° per minute from 2° to 60° using a $\text{CuK}\alpha$ target X-ray tube with an acceleration voltage of 30 kV and a filament current of 16 mA. A randomly oriented sample and an oriented sample were prepared for each fraction. Ethylene glycol and HCl treatments were applied to all fractions to determine clay mineral species.

The mineralogy of individual ash particles was investigated by stereoscopic microscope observation (on particles $>125 \mu\text{m}$) and SEM-EDS semi-quantitative analysis focusing on textures, shapes, color, and chemical composition. The ash morphology was observed using stereoscopic microscope and a scanning electron microscope (SEM, JSM-6610LV with a tungsten filament; JEOL Co.) at Akita University. Semi-quantitative microprobe analysis was carried out with an energy-dispersive X-ray spectroscopy (EDS, INCA X-act; Oxford Instruments) attached to the SEM. Semi-quantitative analysis was carried out at an acceleration voltage of 15 kV, a probe current of 2.2 nA, a working distance of 10 mm, and a live time of 20 seconds. Polished sections were prepared for the SEM-EDS observation on the coarse and medium fractions. Atomic proportions measured by SEM-EDS semi-quantitative analysis were used to specify mineral species combined with XRD measurement on bulk samples. Analytical accuracy and precision of the semi-quantitative SEM-EDS analysis were reported by Ohba et al. (2011), indicating precisions less than 0.3 wt% and consistency with WDS analysis for major elements in plagioclase, olivine, and pyroxenes.

3.5. Results

3.5.1. Minerals in the ash

Minerals identified in the ash are listed in Table 3.1. The XRD measurement elucidated that smectite, pyrophyllite, mica, a 7-Å kaolin group mineral (any of kaolinite, nacrite, or dickite), quartz, cristobalite, alunite, gypsum, and pyrite occur in all fractions. The X-ray peaks of quartz, 7-Å kaolin group minerals, alunite, and gypsum are sharp and their intensities are high in both fractions. Feldspar and anhydrite only occur in the coarse and the medium fractions. The intensities of X-ray peaks of the sheet silicate minerals are higher in the fine fraction than in other fraction.

SEM-EDS microprobe analysis was carried out to identify mineral species in individual grains of the medium and coarse fractions. There is no mineralogical difference between the coarse and medium fractions except for the presence of calcium sulfate minerals in the medium fraction. Each ash grain consists mostly of multiple mineral crystals ranging from submicron to millimeter in size. The EDS analysis on very fine crystals sometimes yields confusing results because the induced X-rays from adjacent crystals affect those of the target crystal (e.g., analysis on a mixture of fine crystals of quartz and kaolin may result in deceptive composition similar to pyrophyllite). To reduce this effect, only crystals that are compositionally and texturally homogeneous were analyzed. Some grains exhibit apparently homogeneous textures, although these consist of very fine crystals (smaller than the resolution of the image). The compositional homogeneity was examined by repeating the analysis on multiple positions in the grain. If a grain that is even apparently homogeneous is a mixture of different fine crystals, elemental proportion arbitrarily changes by position.

The following minerals were identified with SEM-EDS based on stoichiometric relations: silica mineral (SiO_2), pyrite (FeS_2), and alunite

$((\text{Na,K})\text{Al}_3(\text{SO}_4)_2(\text{OH})_6)$ were determined simply on the basis of analytical values close to these ideal chemical formulae. Here we use the term "silica mineral" because identification of silica polymorphs is often impossible with EDS analysis. Fine alunite crystals interweaved with silica mineral show spectra imposed by Si peaks, which can be still identified as the mixture of these minerals based on their distinct elemental proportions. Similarly, rutile that occurs as tiny crystals mixed with silica minerals is identified from distinct titanium spectra accompanied by silica peaks with arbitrarily changing intensity. As two types of calcium sulfate minerals were identified with XRD, gypsum and anhydrite are distinguished by the oxygen/sulfur ratio. Feldspar, pyroxene, and garnet were identified with stoichiometric proximities between the ideal formulae and the analytical results. Results for the very fine feldspar yielded X-ray spectra influenced by juxtaposed crystals, resulting in discrepancy from the ideal formula, and were discarded. Spectra with SiO_2 and Al_2O_3 indicate the presence of hydrous aluminous silicate mineral (either pyrophyllite or kaolin group minerals). Pyrophyllite consists mostly of Al_2O_3 and SiO_2 and the atomic concentration of Si is twice that of Al. It contains minor amounts (<2 wt%) of MgO, K_2O , FeO, and CaO. Kaolin-group mineral is characterized by the chemical formula wherein the atomic concentrations of Si and Al are the same. Kaolin frequently occurs as very fine crystals inwrought with silica mineral, resulting in a deceptive spectrum with higher silica concentration than kaolin. The spectra were identified as a mixture of silica and kaolin when multiple analyses on different position yielded varying Al/Si ratios which can exceed 0.5. Chlorite was identified from spectra comprising distinct Si, Al, Mg, Fe peaks and negligible peaks of Na, K, and Ca if the total of cations is 20 when the number of oxygen is assumed to be 28. Mica minerals are characterized by an abundance of SiO_2 , Al_2O_3 , and K_2O and can be distinguished from potassium feldspar by their stoichiometry. Mica was identified when the mineral has two potassium when oxygen number is assumed to be 22. Muscovite is the most common mica mineral in the sample. The simple

Table 3.1 Minerals in the volcanic ash of the 2014 eruption at Ontake volcano

Fraction	Qtz	Crt	Trd	Fsp	Smct	Opx	mica	Pyl	Kao	Pyr	Alu	Anh	Gyp
Bulk	***	**	f	**	f	***	f	f	*	*	***	f	**
Coarse	***	***	*	**	f	***	f	f	*	***	*	f	*
Medium	***	**	f	***	f		f	f	***	**	**	***	*
Fine	***	f			**	f	**	f	***	f	***		***

The intensities of X-ray peaks in the XRD analysis are shown as: ***: intense; **: weak; *: minor; f: faint and blank none.

The minerals are; Qtz: Quartz, Crt: Cristobalite, Trd: Tridymite, Fsp: Feldspars, Smct: Smectite, Opx: Orthopyroxene, mica: mica minerals, Pyl: Pyrophyllite, Kao: 7 Å-kaolin group mineral, Pyr: Pyrite, Alu: Alunite, Natroalunite and Minamiite, Ahd: Anhydrite, and Gyp: Gypsum.

chemical formula of muscovite is $\text{KAl}_2(\text{Si}_3\text{Al})\text{O}_{10}(\text{OH})_2$, in which potassium can be partly replaced by sodium and calcium, and the octahedral aluminum by iron, manganese, magnesium, and titanium. Mica mineral rich in Fe and Mg is regarded as biotite.

3.5.2. Mineralogy and petrography of individual ash grain

Ash grains in the coarse fraction have various appearances under a binocular microscope; opaque white-colored grains, opaque gray-colored grains, translucent brownish gray-colored grains, translucent white-colored grains, transparent grains, and free crystals (Fig 3.2). Various kinds of altered rock fragments were observed with SEM-EDS. The ash grains are classified into seven types according to mineral assemblages: partly altered volcanic rock fragment, silica mineral - pyrite, silica mineral - pyrite \pm alunite \pm kaolin-group mineral, silica mineral - pyrophyllite - pyrite, silica mineral - pyrophyllite - pyrite, silica mineral - muscovite, silica mineral - K-feldspar \pm albite \pm garnet \pm biotite, and crystals of pyrite, anhydrite, and gypsum (Table 3.2). The complete table of the mineral assemblages is included in the supplemental material (Appendices I).

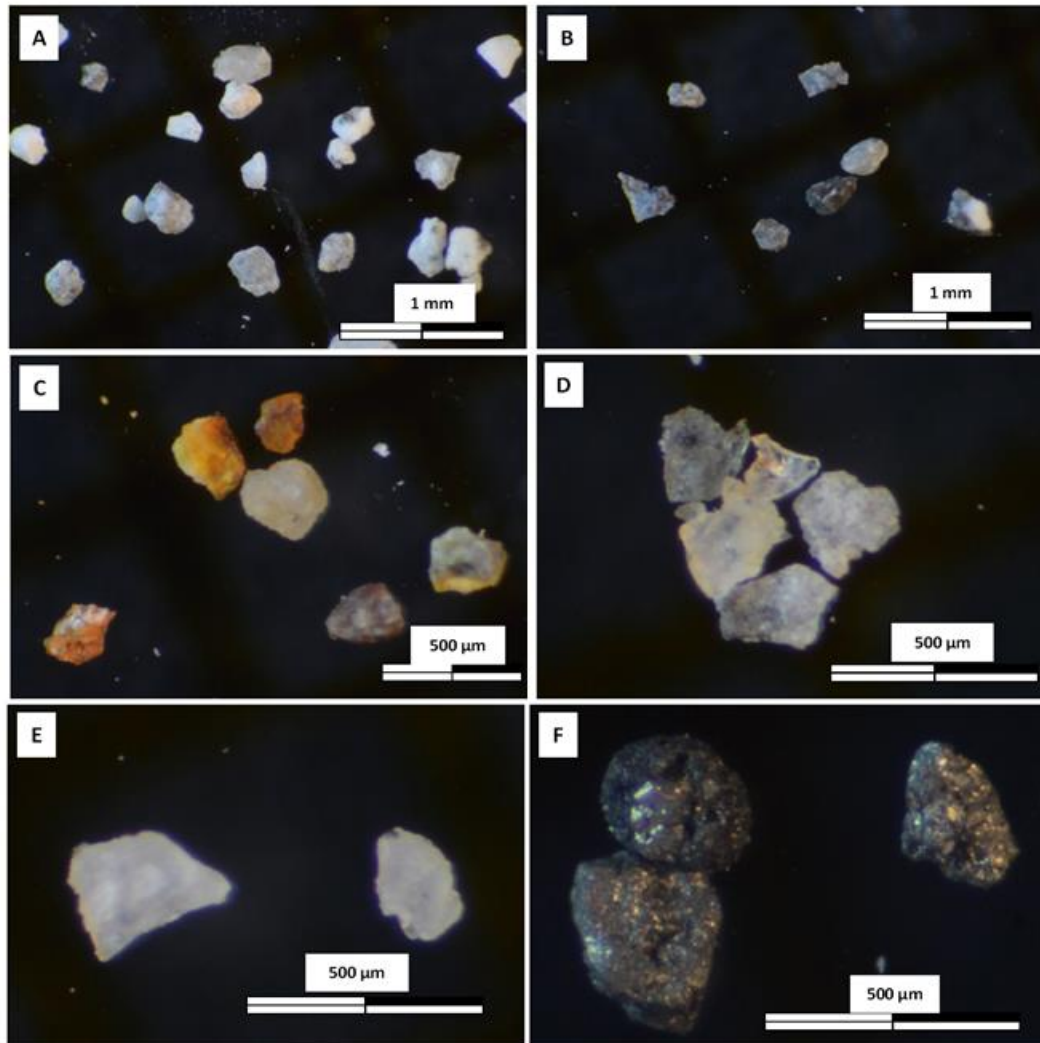


Fig. 3.2. Photographs of ash particles from the 27th September 2014 eruption. (A) Opaque white-colored grains, (B) opaque gray-colored grains, (C) translucent brownish gray-colored grains, (D) transparent grains, (E) translucent white-colored grains, and (F) free crystals of pyrite.

Table 3.2 Mineral assemblages of altered rock fragments in the volcanic ash

Sample name	Mineral assemblages [†]																glass	Alteration ^{††}	Color [‡]
	Si	Ab	Kfs	Kao	Mus	Pyl	Alu	Anh	Pyr	Chr	Rul	Pl	Ano	Px	Bi	Grt			
141014 coarse-6	*			*					*			*	*	*			*	partly	nd
Med3-4-7			*									*						partly	nd
Coase-1	*								*		*							RS	OW
Coarse-11	*										*							RS	OG
Coarse-18	*								*		*							RS	Tr
Coarse-2	*			*					*									AA	OW
Coarse-12	*			*			*		*									AA	OW
Coarse-13	*			*					*									AA	OG
Coarse-14	*						*		*									AA	OG
Coarse-16	*							*	*									AA	OG
Coarse-17	*							*	*									AA	Tr
Coarse-4	*		*		*					*								Ser	TBG
160223 Coarse 4-3	*				*				*									Ser	OW
Coarse-6	*	*	*															PA	TW
Med3-5-10		*	*					*							*			PA	nd
Med 1-2	*		*						*							*		PA	nd

[†]: Mineral names are abbreviated as: Si: Silica mineral, Ab: albite, Kfs: potassic feldspar, Kao: 7 Å-kaolin group mineral, Mus: muscovite, Pyl: pyrophyllite, Alu: alunite, Anh: anhydrite, Pyr: pyrite, Chr: chlorite, Rul: rutile, Pl: plagioclase, Ano: anorthoclase, Px: pyroxene, Bi: biotite, and Grt: garnet.

^{††}: Abbreviations are: Partly: partly altered volcanic rock; RS: residual silica; AA: advanced argillic; Ser: Sericite; and PA: potassic alteration.

[‡]: Abbreviations are: OW: opaque white-colored; OG: opaque gray-colored; TW: translucent white-colored; TBG: translucent brownish gray-colored; Tr: transparent; and nd: no data.

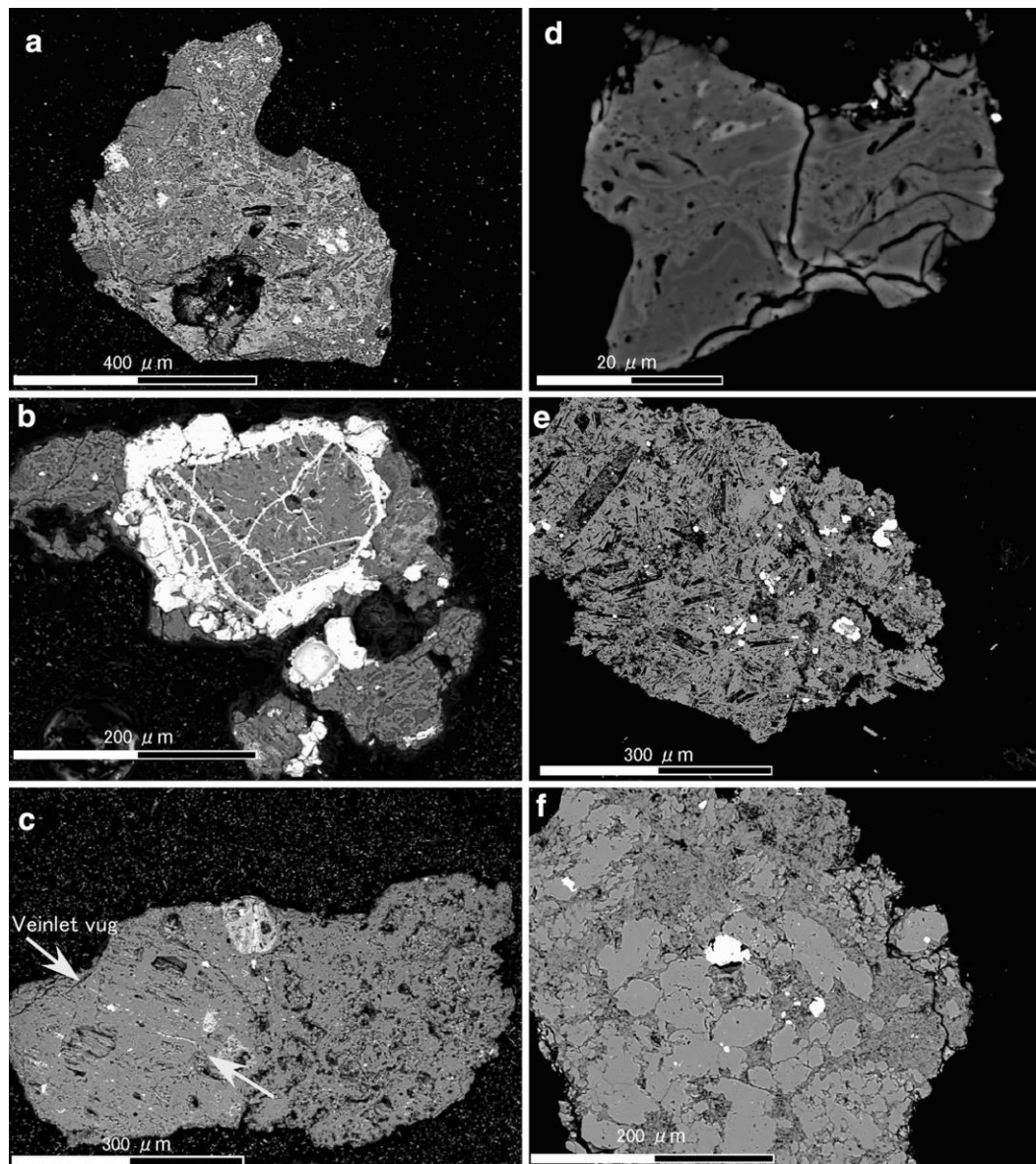


Fig. 3.3. BEI images of volcanic ash particles. (a) Typical partly altered volcanic fragments in the coarse fraction containing microlites of plagioclase, anorthoclase, sanidine, and minor interstitial glass. Some of plagioclase microlites and glass were replaced by pyrite, silica mineral, kaolin-group mineral, and muscovite. (b) The silica - pyrite assemblage in a grain containing darker pseudomorph in the matrix. Pyroxene phenocryst is replaced by silica mineral, and pyrite crystals fill the cleavage of the pseudomorphs. (c) The right side of the grain partly retained the original vesicular texture, while the left part shows a completely deformed texture. Narrow veinlets of vug and pyrite crystals are recognized in the deformed part (arrow). (d) Grains containing silica - pyrite assemblage with colloform texture consisting of micron-width wavy bright bands and darker matrix. (e) Grain consisting of silica mineral, pyrite, alunite, kaolin-group mineral, showing pseudomorphic volcanic texture. Original crystals were replaced by silica mineral or kaolin (darker) or became void. (f) A silica minerals - pyrophyllite - pyrite assemblage grain comprises anhedral silica crystals (gray) and a fine-grained matrix of pyrophyllite (darker).

3.5.2.1. Partly altered volcanic rock fragment

Partly altered volcanic fragments are common in the ash, occurring as angular to subangular blocky fragments of partly altered volcanic rocks and minerals comprised of plagioclase, orthopyroxene, and magnetite. The partly altered rock fragments preserve the texture of volcanic rocks containing volcanic glass. Isolated crystals of plagioclase and orthopyroxene are inferred to be derived from volcanic rocks because they contain glass inclusions. Volcanic rocks of the cone are the source of the minerals, which contain them as phenocrysts (Yamada and Kobayashi, 1988). Two types of groundmass-derived fragments were identified: one consisting of abundant volcanic glass and minor microlites of plagioclase and pyroxene that form hyalo-ophitic texture, and the other one consisting of microlites of plagioclase, anorthoclase, and sanidine, and minor interstitial glass that form hyalopilitic texture (Fig. 3.3A). The original igneous minerals and glass are partly replaced by pyrite, silica mineral, kaolin-group mineral, and muscovite.

3.5.2.2. Silica mineral - pyrite

This association consists dominantly of silica mineral, subordinate pyrite, and minor rutile. Grains of this association are abundant in the ash. They appear opaque white under a binocular microscope. This association includes various textures: pseudomorphic replacement of original volcanic rock textures (Fig. 3.3B), colloform texture, and mosaic-texture. The grains are composed of silica minerals, minor pyrite, and rutile. The pseudomorphic textured grains preserve the original volcanic rock textures, although the original minerals have been completely replaced, mostly by silica mineral. The grains are rich in voids that are spherical, tabular, veinlet, and irregular in shape. The voids range from submicron to hundreds of μm in size, and small voids often form spongy textures.

Pyrite crystals frequently fill the voids and the cleavage of the pseudomorphs of phenocrysts (Fig. 3.3B, C).

The pores in the highly porous grains are spherical, tabular, vein-like and irregular in shape, and range from several hundred to just a few micro meters (Fig. 3.3C). The spherical pores are larger than the other types and have diameters of several hundred μm . Tabular-shaped pores typically range from few tens to few μm . The grains with colloform texture consist of micron-width wavy bright bands and darker matrix on BEI (Fig. 3.3D). The colloform grains contain void veins and irregular-shaped pores (Dong et al., 1995; Fig. 3.3D). Mosaic-textured grains consist of tens- μm -sized equant interlocking quartz crystals. The crystalline rock fragments contain pores ranging from submicron to tens of μm .

3.5.2.3. Silica mineral - pyrite \pm alunite \pm kaolin-group mineral

The association of silica mineral - pyrite \pm alunite \pm kaolin-group mineral is the most common of the ash grains. Grains with this assemblage appear as opaque white-colored or opaque gray-colored under a binocular microscope. The original minerals have been completely replaced by silica mineral, alunite, kaolin-group mineral, rutile, and pyrite through hydrothermal alteration. The grains are classified into three types according to textures: pseudomorphic volcanic texture, fine-grained texture, and coarse mosaic texture. Grains with pseudomorphic volcanic texture are rich in vugs and preserve textures of the original volcanic rocks that are porphyritic, hyalo-ophitic, or hyalopilitic. Some vugs are rectangular in shape, indicating that the original crystals had been shed during the alteration, although some crystals have been replaced by silica mineral or kaolin (Fig. 3.3E). Other vugs are spherical, vein-like and irregular in shape, ranging from a few to several hundred μm . Pyrite and alunite crystals fill some of the vugs and cleavages of the pseudomorphic crystals. Grains with fine-grained texture show no sign of original rock texture but merely consist of fine-grained crystals. These grains are rich in μm -size vugs that are spherical or irregular, and

contain densely distributed submicron vugs forming a spongy texture. The coarse mosaic texture consists of tens to μm -sized equant silica, euhedral to anhedral alunite, and intercrystalline voids. Flaky or massive crystals of alunite fill some of the voids.

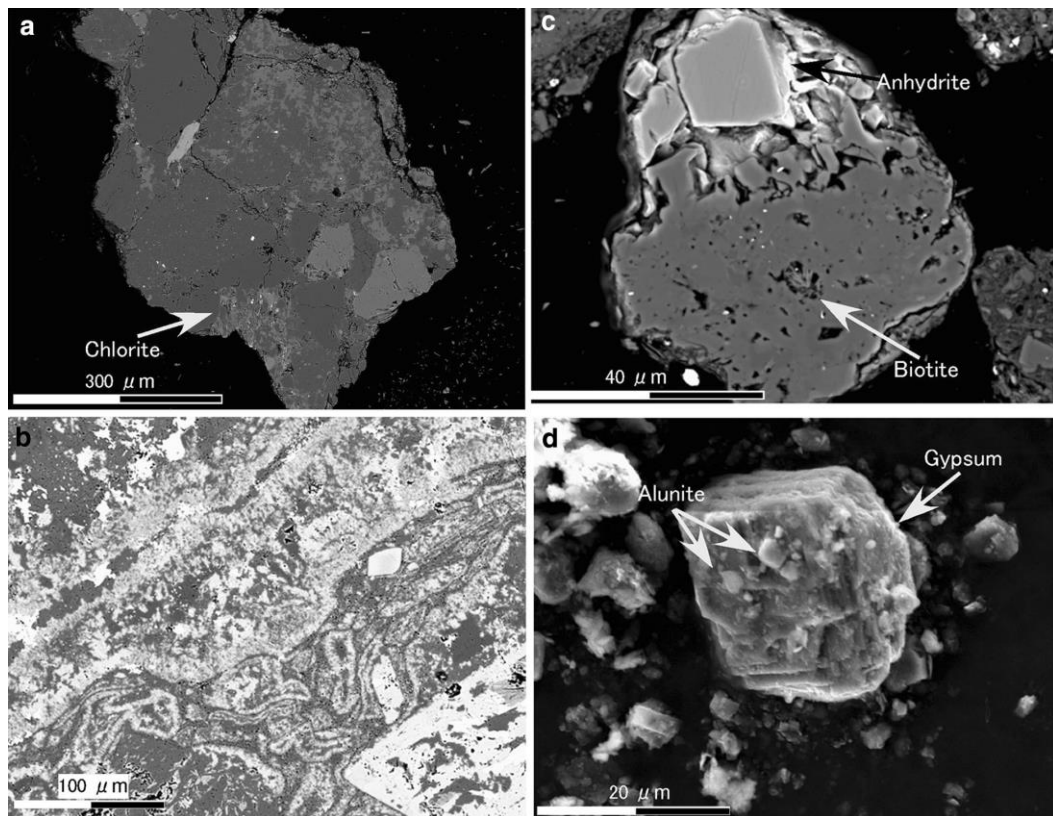


Fig. 3.4 BEI images of volcanic ash particles. (a) A grain consisting of coarse equant crystals of silica mineral, K-feldspar, and albite, forming equigranular texture, partly replaced by diffusively mottled chlorite and muscovite. (b) Colloform texture in a grain consisting of silica minerals–K-feldspar. The colloform texture consists of K-feldspar-rich bands (brighter) and a fine-grained mixture of silica mineral and K-feldspar (darker). (c) Grain of altered rock that belongs to the silica–K-feldspar \pm albite \pm garnet \pm biotite assemblage in the medium fraction. The porous equigranular texture consists of tens- μm -sized equant crystals of silica mineral, K-feldspar, and albite (darker). Anhydrite crystals (bright) are attached conjugate with the grain. (d) The fine fraction consists of free euhedral crystals of alunite and gypsum.

3.5.2.4. Silica minerals - pyrophyllite - pyrite

The association of silica minerals, pyrophyllite, and pyrite is common, occurring as opaque gray-colored or transparent grains. The original texture is completely lost and the original minerals have been replaced by silica mineral, pyrophyllite, pyrite, and minor rutile. Some grains comprise anhedral silica crystals and fine-grained matrix of pyrophyllite (Fig. 3.3f). The silica mineral grains range from 1 to 100 μm in size. Some silica grains contain abundant micron-sized spherical pores. The matrix pyrophyllite occurs as an aggregate of fine flaky crystal or very fine spongy texture dotted with euhedral pyrite crystals. The very fine matrix contains alligating voids. Some pyrophyllite-bearing grains consist solely of very fine-grained pyrophyllite with such voids.

3.5.2.5. Silica minerals - muscovite

The association of silica mineral – muscovite is common in the ash. The ash grains appear as opaque white grains under a binocular microscope. The original rock texture has been lost and the minerals have been totally replaced by a mixture of fine crystals of silica mineral, muscovite, pyrite, and rutile. A peculiar muscovite-bearing grain, which appears as a translucent brownish gray-colored grain, contains chlorite and K-feldspar. The grain consists of coarse equant crystals of silica mineral, K-feldspar, and albite, forming equigranular texture, partly replaced by diffusively mottled chlorite and muscovite (Fig. 3.4a).

3.5.2.6. Silica minerals - K-feldspar \pm albite \pm garnet \pm biotite

The association of silica mineral - K-feldspar - albite - garnet occurs commonly in the ash. Grains with this assemblage appear as translucent white under a binocular microscope. Grains in this association are subdivided two types based on textures: the colloform texture (Dong et al., 1995: Fig 3.4b) and the porous equigranular texture. The colloform texture consists of K-feldspar-rich bands and a fine-grained mixture of silica mineral and K-feldspar. The original

texture has completely disappeared through replacement of altered minerals. The porous equigranular texture consists of tens- μm -sized equant crystals of silica mineral, K-feldspar, and albite (Fig 3.3b). The equigranular grains contain flaky biotite crystals in pores of the K-feldspar.

3.5.2.7. Crystals of pyrite, anhydrite, and gypsum

Free pyrite crystals are common in all size fractions. Euhedral pyrite crystals typically form aggregates ranging in size from a few micrometers to millimeters. Anhydrite-bearing grains are only observed in the medium fraction. Anhydrite occurs as 20 to 50- μm -size euhedral crystals. Some anhydrite crystals conjugate with grains of altered rock that belong to the silica-pyrite or silica - K-feldspar \pm albite \pm garnet \pm biotite associations (Fig. 3.4c). The fine fraction contains fine ($< 10 \mu\text{m}$) euhedral alunite with hexagonal tabular or platy forms and tens- μm -sized polyhedral crystals of gypsum (Fig. 3.4d).

3.5.3. Compositional variations in alunite crystals

Alunite crystals occur in all fractions of the volcanic ash. Semi-quantitative analyses by using SEM-EDS enable us to discuss compositional variation of alunite crystals, although relative error has not been reported in analysis targeting alunite in SEM-EDS at Akita University. Alunite compositions vary in terms of Na_2O and K_2O contents (Appendices II). Here, we show compositional variations in alunite and natroalunite (or minamiite) crystals (Fig.3.5). We adapted forty dates which have total cation fallen into the range of ideal stoichiometry $\pm 5\%$. The compositions of alunite crystals vary broadly range from 0-10% to 50-60% of $\text{Na}_2\text{O}/(\text{Na}_2\text{O}+\text{K}_2\text{O})$. The compositions of alunite crystals show normal distribution and the composition fall into 20-30% of $\text{Na}_2\text{O}/(\text{Na}_2\text{O}+\text{K}_2\text{O})$ are most abundant.

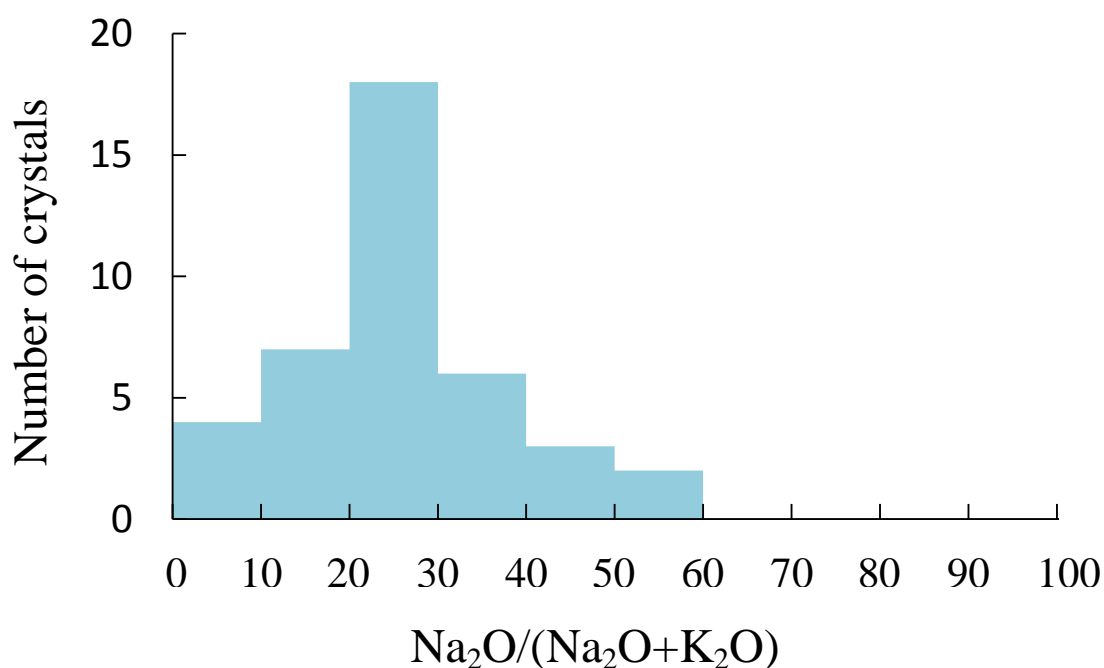


Fig. 3.5 The histogram showing compositional variations in the two end members of alunite and natroalunite.

3.6. Discussion

The volcanic ash is characterized by abundant hydrothermally altered rock fragments with different degrees of alteration and hydrothermally precipitated minerals. Juvenile material such as pumice, scoria, or glass shard was not found in the volcanic ash, whereas partly altered fragments consisting of primary igneous minerals (plagioclase, orthopyroxene, titanomagnetite, and feldspars), volcanic glass, and alteration minerals are common. Therefore, we conclude that the 2014 Ontake eruption was a non-juvenile eruption. Not all feldspars in the ash originate from fresh volcanic rock; some were derived from the alteration zones. Plagioclase, anorthoclase, and alkali feldspar that coexist with volcanic glass in the partly altered volcanic rock fragments originate from fresh volcanic rocks, whereas K-feldspar and albite contained in the altered

fragments of silica mineral - K-feldspar \pm albite \pm garnet \pm biotite association were derived from hydrothermal alteration. Other than the remnant primary minerals, the volcanic ash contains quartz, tridymite, cristobalite, kaolin-group mineral, alunite, anhydrite, gypsum, pyrophyllite, muscovite, chlorite, K-feldspar, biotite, rutile, garnet, pyrite, and smectite. The mineral assemblage is typical of hydrothermal alteration zones in magmatic-hydrothermal systems under subduction zone volcanoes (Rye et al., 1992; Hedenquist and Lowenstern 1994). The mineral assemblages therefore indicate that the volcanic ash was derived from a subvolcanic hydrothermal system developed beneath the edifice of Ontake volcano.

Five associations of alteration minerals were identified from observations on individual grains: silica - pyrite, silica - pyrite \pm alunite \pm kaolin, silica - pyrophyllite - pyrite, silica - muscovite, and silica \pm K-feldspar \pm albite \pm garnet \pm biotite. The ash also contains free crystals of sulfide and sulfate minerals. Detailed mineralogy on these associations gives clues to the hydrothermal alteration processes and conditions. Abundant pores in pseudomorphic volcanic texture of grains from the silica - pyrite and silica - pyrite \pm alunite \pm kaolin associations (Fig. 3.3C, D) were presumably formed by deflection of original crystals such as plagioclase and pyroxene during chemical leaching by highly acidic fluid, although some of pores probably reflect the original vesicular texture typically observed in volcanic rocks. Similar textures have been attributed to steam-heated volcanic environments and high-sulfidation ore systems in previous works (e.g. Giggenbach, 1975; Stoffregen, 1987; Rye et al., 1992). The textures and the dominance of the silica component imply that the silica - pyrite association is the residue of the leaching of other major cations from original rock, which has been termed vuggy silica alteration (Stoffregen, 1987; Hedenquist et al., 2000). The associations of silica - pyrite \pm alunite \pm kaolin and silica - pyrophyllite - pyrite shows textural evidence similar to advanced argillic type of alteration (Stoffregen, 1987; Sillitoe, 2010), wherein cations other than Al and Si

are leached and accompanied by sulfate and sulfide precipitation. Two types of alteration that precipitate K-feldspar are suggested by the mineralogy of individual grains of the association of silica - K-feldspar \pm albite \pm garnet \pm biotite. The occurrence of flaky biotite in the pores of the equigranular ash grains indicates that this mineral precipitated from fluid. The paragenesis of K-feldspar (alkali feldspar with Or40-60) and the biotite represent full equilibration between a near-neutral hydrothermal fluid and host rock at high temperature (>300 °C) (Giggenbach, 1997), referred to as potassic alteration (Meyer and Hemley, 1967). On the other hand, the colloform grains that lack biotite and the composition of the colloform-forming K-feldspar is the near-end member (Or >97) which represents low temperature crystallization. The K-feldspar colloform texture resembles typical altered rocks in hydrothermal veins of epithermal ore deposits (Fournier, 1985; Saunders, 1990). These characteristics imply that the colloform texture of this association was formed under full equilibrium conditions at low temperature (<250 °C; Faure et al., 2002) in an epithermal environment.

The altered rock fragments in the ash indicate that the volcanic ash particles of the 2014 eruption of Ontake volcano were derived from different alteration zones distributed underneath the crater, including zones formed at a highly acidic condition (vuggy silica and advanced argillic zones) and at near-neutral conditions (sericite and potassic alterations). Although these zones could be distributed randomly, comparison with systematic spatial distribution models is worthwhile, because many studies have reported distribution models from different perspectives. The distribution models are based on studies of alteration zones surrounding porphyry copper ore deposits (e.g. Sillitoe, 1973, 1999, 2010; Sillitoe and Gappe, 1984; Giggenbach, 1997), active volcanoes (e.g. Ohba and Kitade, 2005; John et al. 2008), and geothermal fields and epithermal ore deposits (e.g. Hemley and Ellis, 1983; Stoffregen, 1987; Heald et al., 1987; Giggenbach, 1997; Hedenquist et al., 2000).

These models commonly involve a silica-rich zone (vuggy silica), with accompanying aluminous hydrous sheet-silicate minerals (kaolin and pyrophyllite) and alunite (advanced argillic alteration zone, lithocap) in the center-top of a system. As applied to the porphyry copper model (Sillitoe, 2010), the silica - pyrite, silica - pyrite \pm alunite \pm kaolin, and silica - pyrophyllite zones are correlated with vuggy residual quartz/silicification, quartz - alunite and quartz - kaolinite zones, and the quartz - pyrophyllite zone, respectively. The association including K-feldspar implies hydrothermal alteration at near-neutral conditions, which can occur at different locations in hydrothermal systems. Some studies on volcanoes have found that neutralization of hydrothermal fluid tends to progress outward from the silicic core (vuggy silica alteration zone) through advanced argillic and argillic zones to propylitic alteration zones (Mt Shimokura: Ohba and Kitade, 2005; Mt Rainier: John et al. 2008) by analogy to the zonation in geothermal areas and epithermal ore fields (e.g. Hemley and Ellis, 1983; Kimbara, 1983; Stoffregen, 1987; Heald et al., 1987; Hedenquist et al., 2000). In those contexts, the propylitic alteration zone represents near-neutral conditions. On the other hand, neutralization in porphyry copper systems occurs below the advanced argillic alteration zone, and this type of alteration is referred to as potassic alteration (Giggenbach, 1997; Sillitoe, 2010). The paragenesis of alkali-feldspar and hydrothermal biotite in the volcanic ash indicates high-temperature neutralization. This seems more likely to reflect the potassic alteration typical of porphyry copper systems, rather than neutralization at low temperature to form propylitic alteration that accompanies chlorite precipitation (Giggenbach, 1997). According to the geologic models for porphyry copper systems, the potassic zone is located under the advanced argillic alteration zone (Giggenbach, 1997; Sillitoe, 2010). The Ontake volcanic ash contains few grains indicating the K-feldspar-bearing alteration (colloform texture) that potentially represents low temperature conditions typical of epithermal ore deposits (Fournier, 1985; Saunders, 1990). The low-temperature neutral alteration might be locally distributed at shallow

levels. The common occurrence of the silica-muscovite association supports a correlation between the volcanic ash and deep-seated neutral zones. In porphyry copper models, this association can be correlated with the sericite zone located between the silica-pyrophyllite zone and the potassic zone. We conclude that the volcanic ash of the 2014 Ontake eruption was derived from the magmatic-hydrothermal system that correlated well with the models for the porphyry copper system.

Here, the source depths of the volcanic ash particles are roughly estimated by correlating with the porphyry copper model by Sillitoe (2010), which shows a geologic structure in the late stage of porphyry system development. A late-stage porphyry system beneath Ontake volcano is assumed based on the association of alteration zones and the occurrence of anhydrite crystals attached to the grains of the silica - pyrite and silica - K-feldspar \pm albite \pm garnet \pm biotite associations. These occurrences are interpreted as fragments of altered rocks cut by anhydrite veinlets that represent a late-stage porphyry system (Fig. 3.6; Sillitoe, 2010). In the model, the residual silica zone occurs from the surface to \sim 1 km depth. The advanced argillic alteration zone ranges from the surface to \sim 2 km (quartz-alunite zone: surface to \sim 1 km; quartz-pyrophyllite zone: \sim 1 to \sim 2 km). The sericite zone is situated at depths between \sim 1.5 and \sim 2 km, and the potassic zone is located deeper than \sim 2 km. Therefore, this correlation shows that the maximum source depth is \sim 2 km, but that the ash from shallow levels (\sim 2 km to near the surface) is more abundant. The depths of hypocenters linked to the eruption are shallower than 3.5 km (Kato et al., 2015; Maeda et al., 2015). The shallow focal depths ($<$ 3.5 km) are roughly consistent with the source depths of volcanic ash.

Some types of ash grains are not involved in the correlation with porphyry copper models. The K-feldspar in the colloform-texture grains has Or-endmember compositions that imply precipitation from low-temperature neutral fluid under epithermal conditions (Fournier, 1985; Saunders, 1990; Giggenbach,

1997). Because epithermal alteration commonly develops at shallow levels above a deeper porphyry copper system (Henley and Ellis, 1983; Sillitoe, 1989, 2010; Giggenbach, 1997; Sillitoe and Hedenquist, 2003), the colloform-texture ash is under evidence of a shallow epithermal system overlying a deep porphyry system under Ontake volcano. Gypsum occurrence has been commonly reported from porphyry copper systems (e.g. Sillitoe, 1973; Hezarkhani et al., 1999; Li et al., 2011), but has not been assigned in the mineral zonation model. Accordingly, we are not able to correlate gypsum occurrence with the model.

The validity of the model adoption for the subvolcanic hydrothermal system can be challenged by locus and temperature estimation based on pyrophyllite stability region. Temperatures relating to formation of hydrothermal minerals can be estimated from the extensively studied phase equilibria of the $\text{Al}_2\text{O}_3\text{-SiO}_2\text{-H}_2\text{O}$ and its extended systems (Helgeson et al., 1978; Hemley et al., 1980; Chatterjee et al., 1984; Anovitz et al., 1991; Berman, 1988; Sverjensky et al., 1991). The common occurrence of pyrophyllite, kaolin, and quartz in the volcanic ash can be applied to these phase equilibria. Previous studies have elucidated that the mineral occurrences at low pressure relate to the reactions:

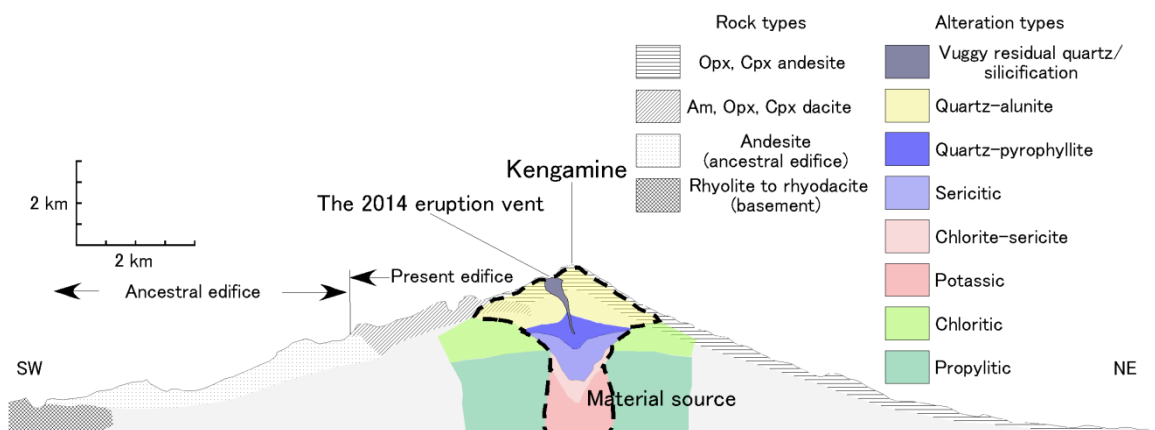
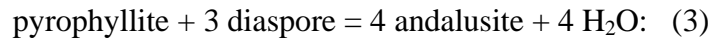
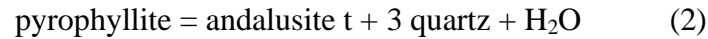
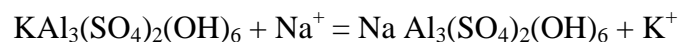


Fig. 3.6 Cross-section of Ontake volcano showing models of basement rock types, ancestral and present edifice based on Yamada and Kobayashi (1988). Alteration zones underlying the edifice are modified from Sillitoe (2010) to estimate the source depth of the volcanic ash. The dashed line indicates possible regions of the source of the volcanic ash.



Equilibrium temperatures under water-saturated condition are: >260 °C for (1); >340 °C for (2); and >310 °C for (3) (Hemley et al., 1980). Hydrothermal temperatures of >260 °C are thus feasible under volcanic condition. Vapor pressure of pure water is higher than 3 MPa and locus of the fluid is estimated deeper than 300 m from surface (Hemley et al., 1980, Fisher and Zen, 1971). These results are feasible to the locus estimated by correlation with porphyry copper system.

Temperature of the source fluid can be discussed chemical compositions of alunite solid solution as well. Alunite s.s. formed over a wide temperature and pH ranges from volcanic to weathering environments and their compositions vary reflecting forming environments (Aoki, 1991; Stoffregen and Alpers, 1992). An experimental study done by Stoffregen and Cygan (1990) demonstrated that (1) the equilibrium constant for the reaction



decreases with decreasing temperature; (2) alunite and natroalunite are completely miscible down to at least 350 °C; and (3) alunite and natroalunite form asymmetric solid solution below 450 °C. Stoffregen and Cygan (1990) also predicted that consolute composition of alunite s.s. as 64.5 mol% natroalunite.

Compositions of alunite s.s. in the volcanic ash vary from 0-10% to 50-60% of Na₂O/(Na₂O+K₂O). We cannot refer to absolute temperature because of all of the compositions of alunite s.s. we obtained are below 64.5 mol.% natroalunite (Fig. 3.5). Whereas, broadly compositional range of alunite s.s. in the volcanic ash may suggest that they were formed under multiple environments.

3.7. Conclusions

The volcanic ash of the eruption on 27th September 2014 at Ontake volcano was derived from the magmatic-hydrothermal system developed beneath the edifice. The mineralogy of the ash grains indicates the development of

advanced argillic, sericite, and high-temperature potassic alteration zones. Associations of these alteration zones are correlated with those in late-stage porphyry copper systems. The comparison with the porphyry copper system estimates the depths of the advanced argillic, sericite, and potassic zones as 0 to ~2 km, ~1.5 to ~2 km, and > 2 km, respectively. Therefore, the ash particles were derived from a maximum of ~2 km depth, and mainly from shallower levels (~2 km to near the surface).

CHAPTER IV. DISCUSSION

Lahar is a remobilization process in a volcano in terms of mass-transportation (Newhall and Punongbayan, 1996). Accordingly, a resultant deposit of a lahar consists of their parent materials, which are any or all of pyroclastic, autoclastic, and epiclastic deposits on a volcanic flank (Vallance and Iverson, 2015). As many lahars were caused by volcanic activities (e.g. the 1985 eruption of Nevado del Ruiz (Pierson et al., 1990); the 1980 eruption Mount St Helens (Scott, 1988); and the 1991 eruption of Pinatubo (Vallance and Iverson, 2015)), lahar deposits consists mainly of deposits resulting volcanic activities which caused lahars. Componential features of a lahar deposit, therefore, enable us to discuss causes volcanic activities.

Origin and triggering mechanisms of the muddy lahars can be explained two types of deriving mechanisms: (1) hydrothermally altered materials were derived by a landslide from hydrothermally altered zone exposed by edifice-collapse at 2.5ka; and (2) Hydrothermally altered materials were derived by hydrothermal eruptions. The muddy lahar deposits (ND1-8) contain hydrothermally altered minerals of smectite, 7Å-kaolin group minerals, chlorite, alunite, and gypsum (Table. 2.1). The geneses of the muddy lahar deposits cannot be estimated based on the mineral assemblage, because these mineral associations are reported both of hydrothermal or phreatomagmatic eruptions (e.g. Hedenquist and Hemley, 1985; Ohba and Kitade, 2005; Mazot et al., 2008) and collapse-induced lahar deposits (e.g. Carrasco-Núñez et al., 1993; Lecointre et al., 2002; John et al., 2008).

In briefly speaking, collapse-induced muddy (or cohesive) lahar deposits are larger than about 0.2 km³ (Vallance, 2000). On the other hand, Sasaki et al. (2016) summarized volume of syneruptive-spouted type cohesive lahar deposits

and conclude that these are less or equal to about 10^5 m^3 . Sasaki et al. (2016) do not refer lahars induced by ash-fall of hydrothermal eruption. It is probably because these lahars are difficult to district from cohesionless lahars induced by magmatic eruption.

Lahar deposits at the northern foot of Chokai volcano can be subdivided into muddy and sandy in terms of their components. In briefly, muddy lahars occurred at least two periods: one is after edifice collapse at BC 466 until the first sandy lahar occurred (ND1-8: Mitsutani, 2001; Ohzawa et al., 1982); and the other is 1802 (Fig. 2.8), whereas ages of some muddy lahar deposits are not determined. Sandy lahars occurred between 5th-6th BC century and 9th century.

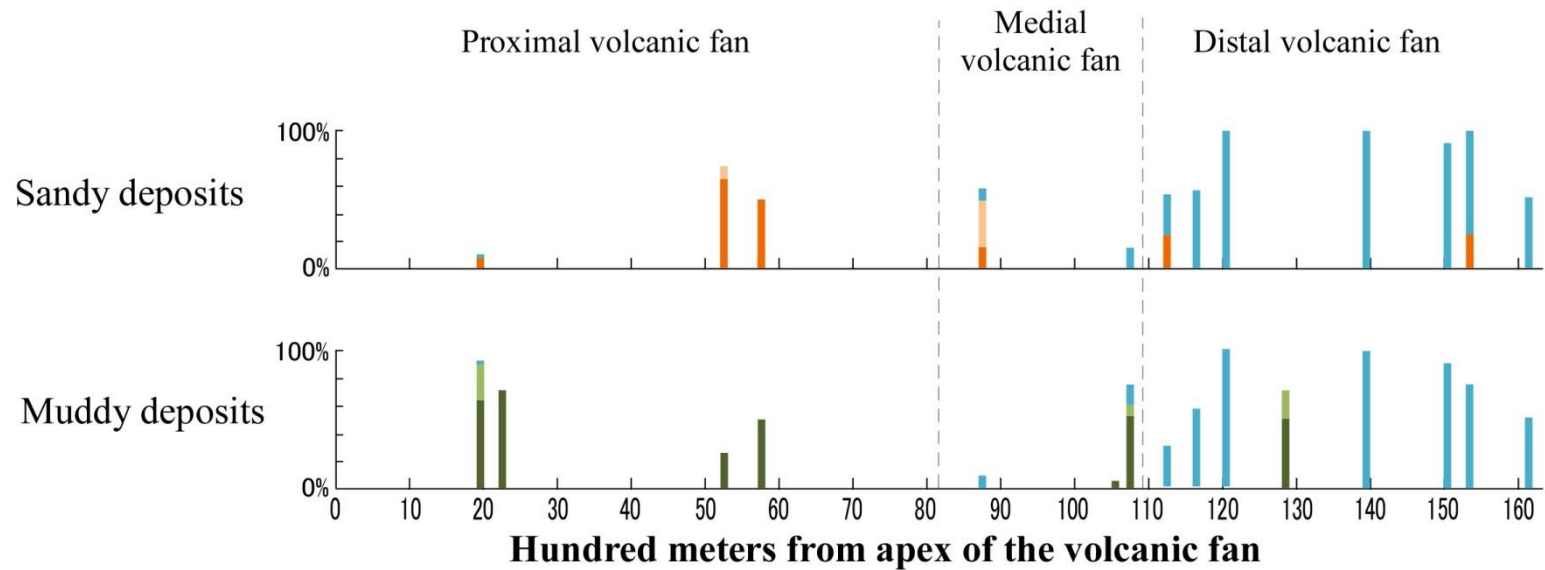
The muddy lahars (ND1-8) in BC466 to the middle of 5th century BC occurred in a short period (less than 100 years). The possibilities of lahar origins collapse-induced and hydrothermal eruption-induced are possible, because of short elapsed time from the collapse. The volume of these lahar deposits can be calculated by their thickness in outcrops (Fig. 2.6) and distribution area. We assume that their distribution area is equal to the area of the proximal volcanic fan. Volume of the muddy lahar deposits ranges from 10^7 to $4 \times 10^8 \text{ m}^3$. This estimated volume closer to deposits of collapse-induced cohesive lahar rather than hydrothermal eruption-induced. The sandy lahars occurred in of 5-6th century BC to 8th – 12th century AD (ND9-16, YK1, YK5, NK2, MR2, MR3, and YN3) contain abundant volcanic sand and poor in hydrothermally altered materials (Table 2.1). These componential features may indicate that they may be induced by magmatic activities after the edifice collapse. As Ohba at al. (2012) reported, Chokai volcano changed their eruption styles from hydrothermally to magmatic after the collapse. Accordingly, the sandy lahars may be induced by any of these magmatic eruptions. The muddy lahar occurred at 1802 (YK5, YK6, NK6, NK2, and HTE3) can be interpreted that was induced by hydrothermal or

phreatomagmatic eruption as reported by Hayashi (2013) and Hayashi and Minami (in printing).

Upward facies changes from debris flow (Dmm and Dmc) to hyperconcentrated flow (Dmb) or sheetflood (Ss) were observed at Loc. 2 (ND1 to ND2 and ND5 to ND6), Loc.4 (ND10 to ND11), Loc. 10 (HTN2 to HTN3), Loc. 11 (KDP2 to KDP3), and Loc.17 (MR1 to MR2). These facies changes indicate the flow transformation at a given location (e.g. Scott, 1988; Smith, 1988; Smith and Lowe, 1991). The hyperconcentrated flow (and sheetflood) deposit overlying debris flow suggests a lahar transform their transportation/deposition process from dense and massive mass-flow to dilute grain-by-grain transportation (Shon et al., 1999; Kataoka and Nakajo, 2000). The lack of paleosol layers between the debris flow and hyperconcentrated (and sheetflood) deposits indicate flow transformation occurred during a lahar flow traveling or at least quite short period. Facies change of debris flow to hyperconcentrated flow were observed in both of muddy (Dmmm, Dcmm, and Dmbm) and sandy (Dmms, Dcms, and Dmbs). These facies changes indicate dilution of a lahar flow can occur in both of muddy and sandy flows.

Figure 4.1 shows relative abundance of facies in aspect from their matrix components. Sheetflood deposits cannot be correlated with denser debris/hyperconcentrated flows because facies Ss is characterized well-sorted sand layer. Accordingly, sheetflood deposits were shown in both of muddy and sandy lahars. Abundance of sandy debris flow facies clearly decreases with distance. Sandy debris flow facies account 50-60% in the proximal volcanic fan and less than 30% in the medial to distal volcanic fan. In the medial volcanic fan, sandy hyperconcentrated flow facies own the highest abundance and accounts 30%. The abundance of muddy debris flow is 20-70% in all portions of the volcanic fan. Muddy hyperconcentrated flow facies accounts 20% in the proximal and distal volcanic fan and less than 10% in the medial volcanic fan.

Fig. 4.1 Diagram illustrating relative abundance of the sedimentary facies of sandy and muddy lahar deposits showing the



variation with the distance from the apex of the volcanic fan. Orange bars: sandy debris flow deposits (Dmms, and Dcms); cream-colored: sandy hyperconcentrated flow deposits (Dmbs); green: muddy debris flow deposits (Dmmm and Dcmm); light green: muddy hyperconcentrated flow (Dmdm); and blue bars sheetflood deposits (Ss).

Abundance of facies Ss is most abundant in the distal volcanic fan and up to 100%.

Flow transformation of lahars was suggested by both of sandy and muddy lahars. Clearly variation of sandy debris flow facies from the proximal to distal fan implies flow dilution of sandy lahars during traveling rather than those of muddy debris flow facies. The high abundance of sandy hyperconcentrated flow facies in the medial volcanic fan may suggest that dilution of sandy lahar occurred in the medial volcanic fan, whereas it observed only at one excavation site. Almost constant abundance of muddy debris flow facies and poor abundance of muddy hyperconcentrated flow facies indicate flow transformation was not effective in muddy lahars. As Vallance (2000) pointed out, flow transformation occurs sandy lahars rather than muddy lahars because clay-poor lahars mix more readily with water and clay-rich lahars are typically much larger. A few pieces of evidence of flow transformation in muddy lahars we described may indicate some small scale muddy debris flows can dilute and transform into more diluted hyperconcentrated flow and possibly sheetflood.

CHAPTER V. CONCLUSIONS

The geomorphology of the volcanic fan at the northern base of Chokai volcano varies with dominant facies of lahar deposits. The distal volcanic fan is characterized by steep gradients ($> 2^\circ$) and by development of lobes and is composed mainly of debris flow deposits. The medial volcanic fan is characterized by moderate gradients ($1^\circ - 2^\circ$) and by diffusive debris lobes and comprises both debris flow and fluvial deposits. The proximal volcanic fan has a near-flat even plain ($<1^\circ$), and is composed mainly of sheetflood deposits and floodplain deposits. The geneses of lahars can be constrained by their compositional characteristics and correlations with volcanic activities. The stratigraphic variation in the matrix component is consistent with the change in matrix mineral assemblage, possibly reflecting changes in the source materials from the volcano. At least 16 units of lahars settled in the proximal volcanic fan, and at least eight of them occurred just after the sector-collapse in 2.5 ka. Some lahars reached the distal volcanic fan as sheetfloods. Such large-scale lahars occurred at least four times, the 5th – 6th century BC, the 5th – 7th century AD, 8th – 12th century AD, and 1801 AD.

The volcanic ash of the eruption on 27th September 2014 at Ontake volcano was derived from the magmatic-hydrothermal system developed beneath the edifice. The mineralogy of the ash grains indicates the development of advanced argillic, sericite, and high-temperature potassic alteration zones. Associations of these alteration zones are correlated with those in late-stage porphyry copper systems. The comparison with the porphyry copper system estimates the depths of the advanced argillic, sericite, and potassic zones as 0 to ~2 km, ~1.5 to ~2 km, and > 2 km, respectively. Therefore, the ash particles were derived from a maximum of ~2 km depth, and mainly from shallower levels (~2 km to near the surface).

Geneses of lahar at the northern base of Chokai volcano was discussed based on their components, volume, and correlation with volcanic activities. Geneses of the muddy lahars were estimated: the edifice collapse induced muddy lahars from BC 466 by the first sandy lahar occurred, and hydrothermal or phreatomagmatic eruption at 1801 induced the other muddy lahar. Sandy lahars occurred 5-6th century BC until 8th – 12th century AD were induced by magmatic eruptions. Flow transformation of lahars was suggested by both of sandy and muddy lahars, although transformation likely occurred in sandy lahars rather than muddy lahars.

REFERENCES

- Anoviz, L.M., Perkins, D., Essene, E.J., 1991. Metastability in near-surface rocks of minerals in the system $\text{Al}_2\text{O}_3\text{-SiO}_2\text{-H}_2\text{O}$. *Clays Clay Miner.* 39:225-233.
- Aoki, M., 1991. Mineralogical features and genesis of alunite solid solution in high temperature magmatic hydrothermal systems. *Geol. Surv. Japan Report.* 277:35-37.
- Ban, M., Hayashi, S., Takaoka, N., 2001. K-Ar dating of the Chokai Volcano, Northeast Japan Arc -A compound volcano composed of continuously established three stratovolcanoes-. *Bull. Volcanol. Soc. Japan.* 46:317-333.
- Berman, R.G., 1988. Internally-consistent thermodynamic data for mineral in the system $\text{Na}_2\text{O-K}_2\text{O-CaO-MgO-FeO-Fe}_2\text{O}_3\text{-Al}_2\text{O}_3\text{-SiO}_2\text{-TiO}_2\text{-H}_2\text{O-CO}_2$. *J. Petrol.* 29:445-522
- Bronk, R.C., 2009. Bayesian analysis of radiocarbon dates. *Radiocarbon,* 51:337-360.
- Capra, L. Macías, J.L., 2000. Pleistocene cohesive debris flows at Nevado de Toluca Volcan, central Mexico. *J Volcanol Geoth Res.* 102:149-168.
- Capra, L. Macías, J.L., 2002. The cohesive Naranjo debris-flow deposit (10 km^3): A dam breakout flow derived from the Pleistocene debris-avalanche deposit of Nevado de Colima Volcano (México). *J Volcanol Geoth Res.* 117:213-235.
- Carrasco-Núñez, G., Vallance, J.W., Rose, W.I., 1993. A voluminous avalanche-induced lahar from Citlaltépetl volcano, Mexico: Implications for hazard assessment. *J Volcanol Geoth Res.* 59:35-46

- Chatterjee, N.D., Johannes, W., Leistner, H., 1984. The system $\text{CaO-Al}_2\text{O}_3\text{-SiO}_2\text{-H}_2\text{O}$: new phase equilibria data, some calculated phase relations, and their petrological applications. *Contrib. Mineral. Petrol.* 88:1-13.
- Cronin, S.J., Neall V.E., Palmer, A.S., Lecointre, J.A., 1997. Changes in Whangaehu river lahar characteristics during the 1995 eruption sequence, Ruapehu volcano, New Zealand. *J Volcanol Geoth Res.* 76:47-61.
- Earthquake Research Institute in the University of Tokyo, 2014. http://www.data.jma.go.jp/svd/vois/data/tokyo/STOCK/kaisetsu/CCPVE/shiryo/130/130_no01.pdf. Accessed 4 March 2016.
- Dong, G., Morrison, G., Jaireth, S., 1995. Quartz texture in epithermal veins, Queensland – classification, origin and implication. *Economic Geology* 90:1841-1856. doi: 10.2113/gsecongeo.90.6.1841
- Faure, K., Matsuhisa, Y., Metsugi, H., Mizota, C., Hayashi, S., 2002. The Hishikari Au-Ag epithermal deposit, Japan: oxygen and hydrogen isotope evidence in determining the source of paleohydrothermal fluids. *Economic Geology* 97:481-498. doi: 10.2113/gsecongeo.97.3.481
- Fisher, J.R., Zen, E-an, 1971. Thermochemical calculations from hydrothermal phase equilibrium data and the free energy of H_2O . *Am. Jour. Sci.* 270:297-314.
- Fournier, R.O., 1985. The behavior of silica in hydrothermal solution. *Reviews in Economic Geology* 2:45-62
- Frank, D., 1983. Origin, distribution, and rapid removal of hydrothermally formed clay at Mount Baker, Washington. U.S. Geological Survey Professional Paper: 1022-E

- Giggenbach, W.F., 1975. The chemistry of Crater Lake, Mt. Ruapehu (New Zealand) During and after the 1971 active period. *N.Z. J. Sci.* 14:951-988
- Giggenbach, W.F., 1997. The origine and evolution of fluids in magmatic-hydrothermal systems In: Barns HL (ed) *Geochemistry of hydrothermal ore deposit*, 3rd edn., John Wiley and Sons, New York
- Hayashi, S., 1984. Geology of Chokai volcano. *J. Japan. Assoc. Mineral. Petrol. Econ. Geol.* 79: 249-265. (in Japanese, with English Abstr.)
- Hayashi, S., 2001. On the lava flows appeared during A.D. 871 eruption of Chokai volcano –The meaning of the two big snakes in the record of “Nihonsandaijitsuroku”-. *Historical Earthquakes.* 17:171-175.
- Hayashi, S., 2012. Reconsideration of the 1801 Eruption at Chokai Volcano, Northeastern Japan. *Abstracts of the Society of Historical Earthquake Studies 2011 Meeting*, 71 (in Japanese)
- Hayashi, S., Ban, M., Ohba, T., 2013. Explosive activity during A.D. 1800-1804 eruption of Chokai volcano. *Historical Earthquakes.* 28:85-90.
- Hayashi, S., Minami, Y., (in printing). Lahar occurred in A.D. 1801 at Chokai volcano. *Memoirs of the Faculty of Education and Human Studies Akita University (Natural Science)*.
- Heald, P., Foley, N.K., Hayba, D.O., 1987. Comparative anatomy of volcanic-hosted epithermal deposits; acid-sulfate and adularia-sericite types. *Economic Geology* 82:1-26. 10.2113/gsecongeo.82.1.1
- Hedenquist, J.W., Henley, R.W., 1985. Hydrothermal eruptions in the Waiotapu geothermal system, New Zealand: Their origin, associated breccias, and relation to precious metal mineralization. *Economic Geology* 80:1640-1668. doi: 10.2113/gsecongeo.80.6.1640

- Hedenquist, J.W., Lowenstern, J.B., 1994. The role of magmas in the formation of hydrothermal ore deposits. *Nature* 370:519-527
- Hedenquist, J.W., Arribas, A., Gonzalez-Urien, E., 2000. Exploration for epithermal gold deposits. *Reviews in Economic Geology* 13:245-277
- Helgeson, H.C., Delaney, J.M., Nesbit, T.W., Bird, D.K., 1978. Summary and critique of the thermodynamic properties of rock-forming minerals. *Am. Jour. Sci.* 278A
- Hemley, J.J., Montoya, J.W., Marinenko, J.W., Luce, R.W., 1980. Equilibria in the system $\text{Al}_2\text{O}_3\text{-SiO}_2\text{-H}_2\text{O}$ and some general implications for alteration/mineralisation processes. *Econ. Geol.* 75:210-228.
- Hemley, R.W., Ellis, A.J., 1983. Geothermal Systems Ancient and Modern: A Geochemical Review. *Earth-Science Reviews* 19:1-50
- Hezarkhani, A., Williams-Jones, A.E., Gammons, C.H., 1999. Factors controlling copper solubility and chalcopyrite deposition in the Sungun porphyry copper deposit, Iran. *Mineralium Deposita* 34:770-783. doi: 10.1007/s001260050237
- Hirose, W., Okazaki, N., Ishimaru, S., Tajika, J., 2007. Mudflow and its deposits occurred by the eruption on March 2006 at Meakandake volcano, Hokkaido, northern Japan. *Rep Geol Surv Hokkaido* 78:57-81 (in Japanese, with English Abstr.)
- Japan Meteorological Agency, 2014. Rep. Coordin. Committee on Prediction of Volcanic Eruption, http://www.data.jma.go.jp/svd/vois/data/tokyo/STOCK/kaisetsu/CCPVE/shiryo/130/130_no01.pdf. Accessed 4 March 2016.
- John, D.A., Sisson, T.W., Breit, G.N., Rye, R.O., Vallance, J.W., 2008. Characteristics, extent and origine of hydrothermal alteration at Mount

Rainer Volcano, Cascades Arc, USA: Implications for debris-flow hazards and mineral deposits. *J. Volcanol. Geoth. Res.* 175:289-314

Kataoka, K., Nakajo, T., 2000. Depositional processes of the debris-flow and hyperconcentrated flow deposits, the Ebisutoge-Fukuda tephra (Karegawa volcanic ash) in the Tokai Group, Plio-Pleistocene boundary, central Japan. *Jour. Geol. Soc. Japan.* 106:897-900.

Kataoka, K.S., Kamino, N., Nagahashi, Y., Kimura, K., 2015. Stratigraphy, chronology and depositional processes of lahar deposits in the Sukawa River System, Adataro Volcano, Northeast Japan. *Bull. Volcanol. Soc. Japan.* 60, 461-475. (in Japanese, with English Abstr.)

Kato, A., Terakawa, T., Yamanaka, Y., Maeda, Y., Horikawa, S., Matsuhira, K., Okuda, T., 2015. Preparatory and precursory processes leading up to the 2014 phreatic eruption of Mount Ontake, Japan. *Earth, Planets Space* 67:111. doi:10.1186/s40623-015-0288-x

Kimbara, K., 1983. Hydrothermal alteration and geothermal systems at the eastern part of Hachimantai. *J. Jpn. Assoc. Mineral., Petrol. Econ. Geol.* 78:479-490 (in Japanese, with English Abstr.)

Lavigne, F., Suwa, H., 2004. Contrasts between debris flows, hyperconcentrated flows and stream flows at a channel of Mount Semeru, East Java, Indonesia. *Geomorphology*, 61, 41-58.

Lecointre, J.A., Vincent, N.E., Cleland, W.R., Warwick, P.M., 2002. The 55- to 60-ka Te Whaiu Formation: a catastrophic, avalanche-induced, cohesive debris-flow deposit from Proto-Tongariro Volcano, New Zealand. *Bull. Vol.* 63:509-525

- Li, G., Li, J., Qin, K., Duo, J., Zhang, T., Xiao, B., Zhao, J., 2011. Geology and Hydrothermal Alteration of the Duobuza. *Resource Geology* 62:99-118. doi: 10.1111/j.1751-3928.2011.00182.x
- Lopez, J.L., Perez, D., Garcia, R., 2003. Hydrologic and geomorphological evaluation of the 1999 debris flow event in Venezuela. In: Rickenmann, D., Chen, C.-L. (Eds.) *Proceedings of the Third International Conference on Debris Flow Hazard Mitigation: Mechanics, Prediction, and Assessment*, Davos, Switzerland, 989-1000.
- Maeda, Y., Kato, A., Terakawa, T., Yamanaka, Y., Horikawa, S., Matsuhira, K., Okuda, T., 2015. Source mechanism of a VLP event immediately before the 2014 eruption of Mt. Ontake, Japan. *Earth, Planets Space* 67:187. doi:10.1186/s40623-015-0358-0
- Mannen, K., Doke, R., Harada, M., Honda, R., Idadera, K., Kikugawa, G., Yukutake, Y., Takenaka, J., 2015. Chronology of the 2015 eruption of Hakone volcano, Japan. *Abstracts of the Volcanological Society of Japan 2015 Fall Meeting*, 40–40 (in Japanese)
- Mazot, A., Bernard, A., Fischer, T., Inguaggiato, S., Sutawidjaja, I.S., 2008. Chemical evolution of thermal waters and changes in the hydrothermal system of Papandayan volcano (West Java, Indonesia) after the November 2002 eruption. *J. Volcanol. Geoth. Res.* 178:276-286
- Meyer, C., Hemley, J.J., 1967. Wall rock alteration at Butte, Montana. *American Mineralogist* 50:1717-1722
- Miall A.D., 2006. *The Geology of Fluvial Deposits Sedimentary Facies, Basin Analysis, and Petroleum Geology* 4th corrected printing. Springer-Verlag Berlin Heidelberg. pp. 582.

- Miall, A., 2010. Alluvial deposits. In: James, N.P., Dalrymple, R.W. (Eds.), *Facies models 4: GEOtext 6*, Geological Association of Canada, St. John's, Newfoundland & Labrador, pp. 105-138.
- Minami, Y., Ohba, T., Hayashi, S., Kataoka, K.S., 2015. Depositional processes and temporal component-change of lahar deposits at the northern foot of Cokai volcano, NE Japan. *Bull. Volcanol. Soc. Japan*, 60, 1-16. (in Japanese, with English Abstr.)
- Mitsutani, T., 2001. *Dendrochronology and Cultural Properties*. Art of Japan, Shibundo Press 421 pp. 98. (in Japanese)
- Mizugaki, S., Mishima, Y., Kikuchi, S., 2001. The sediment disasters and mudflows by the 2000 Eruption of Usu Volcano. *J Jpn Soc Eros Control Eng* 54:47–53 (in Japanese, with English Abstr.)
- Mizuyama, T., 1981. An intermediate phenomenon between debris flow and bed load transport. *Erosion and Sediment Transport in Pacific Rim Steeplands*. International Association of Hydrological Sciences, Christchurch, New Zealand, 212–224.
- Miyagi I, Geshi N, Hamasaki S, Tomiya A., 2014. Volcanic ash particles from Ontake volcano on September 2014. In *Abstracts of the Volcanological Society of Japan the 2014 fall meeting*, Fukuoka University, Fukuoka, 2-4 Nov. 2014 [in Japanese]
- Nakano, S., Tsuchiya, N., 1992. *Geology of the Chokaisan and Fukura district*. With Geological Sheet Map at 1:50,000, *Geol. Surv. Japan*. pp. 138. (in Japanese, with English Abstr.)
- Nakano S, Oikawa T, Yamasaki S, Kawanabe Y., 2014. Distribution of craters and pyroclastic flows generated by eruption of Ontake volcano in September, 2014. In *Abstracts of the Volcanological Society of Japan*

the 2014 fall meeting, Fukuoka University, Fukuoka, 2-4 Nov. 2014 [in Japanese]

Newhall, C.G., Punongbayan, R.S. (Editors), 1996. Fire and Mud: Eruptions and Lahars of Mount Pinatubo, Philippine. Philippine Institute of Volcanology and Seismology and the University of Washington press, Quezon City/Seattle.

Ogiso, M., Matsubayashi, H., Yamamoto, T., 2015. Descent of tremor source locations before the 2014 phreatic eruption of Ontake volcano, Japan. *Earth, Planets Space* 67:206. doi:10.1186/s40623-015-0376-y

Ohba, T., Kitade, Y., 2005. Subvolcanic hydrothermal systems: Implication from hydrothermal minerals in hydrovolcanic ash. *J Volcanol Geoth Res* 145:249-262

Ohba, T., Taniguchi, H., Miyamoto, T., Hayashi, S., Hasenaka, T., 2007. Mud plumbing system of an isolated phreatic eruption at Akita Yakeyama volcano, northern Honshu, Japan. *J. Volcanol. Geotherm. Res.* 161:35-46

Ohba, T., Hayashi, S., Suzuki, S., Kondo, A., Kuzumaki, T., Ogata, T., 2011. Chemical analysis of rock-forming minerals at Akita University: Consistency of quantitative analytical results between SEM-EDX of Faculty of Education & Human Studies and WD-EPMA of Faculty of Engineering & Resource Science. *Scientific and Technical Reports of Graduate School of Engineering and Resource Science, Akita Univ.* 32:1-6 (in Japanese, with English Abstr.)

Ohba, T., Hayashi, S., Ban, M., Kondo, A., Kuzumaki, T., Suzuki, S., Furuki, K., 2012. Eruption history at Chokai volcano during the last 4000 years: Implication from ash layers preserved in peat soil. *Bull. Volcanol. Soc. Japan*, 57, 65-76. (in Japanese, with English Abstr.)

- Ohzawa, A., Ikebe, Y., Arakawa, Y., Tsuchiya, N., Satoh, H., Kakimi, T., 1982. Geology of the Kusakata District (including Tobishima in the Sakata District). Quadrangle Series, Scale 1:50,000, Geol. Surv. Japan, pp. 73. (in Japanese, with English Abstr.)
- Ohzawa, A., Katahira, T., Nakano, S., Tsuchiya, N., Awata, Y., 1988. Geology of the Yashima district. With geological sheet map at 1:50,000, Geol. Surv. Japan. pp. 87. (in Japanese, with English Abstr.)
- Oikawa, T., 2008. Reinvestigation of the historical eruption and fumarolic activity records at Ontake Volcano, central Japan. -Misunderstanding reports about the 774 AD and 1892 AD eruptions-. Bull. Geol. Surv. Japan, 59(5/6):203-21. (in Japanese, with English Abstr.)
- Oikawa, T., Suzuki, Y., Chiba, T., 2014. Eruption history and 2014 eruption of Ontake volcano. Kagaku 84(12):1218-1225 [in Japanese]
- Pack, R.T., 2005. Application of airborne and spaceborne remote sensing method. In Jakob, M., Hungr, O. (Eds.) Debris-flow Hazards and Related Phenomena. Praxis. Springer Heidelberg, pp. 275-289.
- Pierson, T.C., Scott, K.M., 1985. Downstream dilution of a lahar: transition from debris flow to hyperconcentrated streamflow. Water Resources Research. 21:1511-1524.
- Pierson, T.P., Janda, R.J., Thouret, J.C., Borerro, C.A., 1990. Perturbation and melting of snow and ice by the 13 November 1985 eruption of Nevado del Ruiz, Colombia, and consequent mobilization, flow and deposition of lahars. J. Volcanol. Geoth. Res. 41:17-66.
- Pierson, T.C., 1995. Flow characteristics of large eruption-triggered debris flow at snow-clad volcanoes: constraints for debris-flow models. J. Volcanol. Geotherm. Res., 66, 283-294.

- Pierson, T.C., Major, J.J., 2014. Hydrogeomorphic effects of explosive volcanic eruptions on drainage basins. *Annu. Rev. Earth Pl. Sci.*, 42:469-507.
- Reed, H.M., 1997. Hydrothermal alteration and its relationship to ore fluid composition In: Barnes HL (ed) *Geochemistry of hydrothermal ore deposits* 3rd edn., John Wiley and Sons, New York
- Reimer P.J., Bard, E., Bayliss, A., Beck, J.W., Blackwell, P.G., Ramsey C.B., Buck, C.E., Cheng, H., Edwards, R.L., Friedrich, M., Grootes, P.M., Guilderson, T.P., Haflidson H., Hajdas, I., Hatté, C., Heaton, T.J., Hoffmann, D.L., Hogg, A.G., Hughen, K.A., Kaiser, K.F., Kromer, B., Manning, S.W., Niu, M., Reimer, R.W., Richards, D.A., Scott, E.M., Southon, J.R., Staff, R.A., Turney, C.S.M., Plicht J., 2013. IntCal13 and Marine13 Radiocarbon Age Calibration Curves 0–50,000 Years cal BP. *Radiocarbon*. 55:1869-1887.
- Rodolfo, K.S., 1989. Origin and early evolution of lahar channel at Mabinit, Mayon Volcano, Philippines. *Geological Society of America Bulletin*. 101:414-426
- Rose, A.W., Burt, D.M., 1979. Hydrothermal alteration. In: Barnes HL (ed) *Geochemistry of hydrothermal ore deposits* 2nd edn., John Wiley, New York
- Rye, R.O., Bethke, P.M., Wasserman, M.D., 1992. The stable isotope geochemistry of acid sulfate alteration. *Economic Geology* 87:225-262. doi: 10.2113/gsecongeo.87.2.225
- Sasaki, H., Mukoyama, S., Inaba, C., 2006. The Eruption of Meakandake Volcano on March 21, 2006, Hokkaido, Japan. *Bull Volcanol Soc Jpn* 51:347–350 (in Japanese)

- Sasaki, H., Chiba, T., Kishimoto, H., Naruke, S., 2016. Characteristics of the syseruptive-spouted type lahar generated by the September 2014 eruption of Mount Ontake, Japan. *Earth, Planets and Space*. 68:141 DOI 10.1186/s40623-016-0516-z
- Saunders, J.A., 1990. Colloidal transport of gold and silica in epithermal precious-metal systems: evidence from the Sleeper deposit, Nevada. *Geology* 18:757-760.doi.org/10.1130/0091-7613(1990)018<0757:CTOGAS>2.3.CO;2
- Scott, K.M., 1988. *Origins, Behavior, and Sedimentology of Lahars and Lahar-runout Flows in the Toutle-Crowlitz River System*. U.S. Geological Survey, Professional Paper, 1447-A, 74p
- Schmincke, H. -U., 2004. *Volcanism*. Springer, pp. 324p.
- Shultz, W.A., 1984. Subaerial debris-flow deposition in the upper Paleozoic Cutler formation, western Colorado. *Journal of Sedimentary Petrology*. 54:759-772.
- Sillitoe, R.H., 1973. The top and bottoms of porphyry copper deposits. *Economic Geology* 68:799-815. doi: 10.2113/gsecongeo.68.6.799
- Sillitoe, R.H., 1989. Gold deposits in western Pacific island arcs: The magmatic connection. *Economic Geology Monograph*. 6:274-291
- Sillitoe, R.H., 1999. Styles of high-sulphidation gold, silver and copper mineralisation in porphyry and epithermal environments. In: *Pacrim '99 Congress, Bali, indonesia, 1999, Proceedings: Melbourne, Australasian Institute of Mining and Metallurgy*. p 29-44

- Sillitoe, R.H., 2000. Gold-rich porphyry deposits: Descriptive and genetic models and their role in exploration and discovery. *Reviews in Economic Geology* 13:315-345
- Sillitoe, R.H., 2010. Porphyry Copper Systems. *Economic Geology* 105:3-41. doi: 10.2113/gsecongeo.105.1.3
- Sillitoe RH, Gappe IM Jr., 1984. Philippine porphyry copper deposits: Geologic setting and characteristics: Bangkok, Thailand, United Nations ESCAP, CCOP Technical Publication 14
- Sillitoe, R.H, Hedenquist, J.W., 2003. Linkages between Volcanotectonic Settings, Ore-Fluid Compositions, and Epithermal Precious Metal Deposits. *Society of Economic Geologists Special Publication* 10:315-343
- Smith, G.A., 1986. Coarse-grained nonmarine volcanoclastic sediment: terminology and depositional process. *Geological Society of America Bulletin*. 97, 1–10.
- Smith, G.A., 1988. Sedimentology of proximal to distal volcanoclastics dispersed across an active foldbelt: Ellensburg Formation (late Miocene), central Washington. *Sedimentology*. 35:953-977.
- Smith, G.A., Fritz, W.J., 1989. Volcanic influences on terrestrial sedimentation. *Geology*. 17:375-376.
- Smith, G.A., 1991. Facies sequences and geometries in continental volcanoclastic sediments. In: Fisher, R.V., Smith, G.A. (Eds.) *Sedimentation in Volcanic Settings*. SEPM Spec. Publ. 45:109-121.
- Smith, G.A., Lowe, D.R., 1991. Lahars : volcano-hydrologic events and deposition in the debris flow-hyperconcentrated -flow continuum. In:

- Fisher, R.V., Smith, G.A. (Eds.) Sedimentation in Volcanic Settings. SEPM Spec. Publ. 45:59-70.
- Stoffregen, R., 1987. Genesis of acid-sulfate alteration and Au-Cu-Ag mineralization at Summitville, Colorado. *Economic Geology* 82:1575-1591. doi: 10.2113/gsecongeo.82.6.1575
- Stoffregen, R.E., Cygan, G.L. 1990. An experimental study of Na-K exchange between alunite and aqueous sulfate solutions. *Amer. Mineral.* 75:209-220.
- Stoffregen, R.E., Alpers, C.N., 1992. Observation on the unit-cell dimensions, H₂O contents, and D values on mineral and synthetic alunite. *Amer. Mineral.* 77:1092-1098.
- Shohn, Y.K., Rhee, C.W., Kim, B.C., 1999. Debris flow and hyperconcentrated flood-flow deposits in an alluvial fan, northwestern part of the Cretaceous Yongdong basin, central Korea. *Journal of Geology.* 107:111-132.
- Suwa, H., Okuda, S., 1983. Deposition of debris flows on a fan surface, Mt. Yakedake, Japan. *Zeitschrift für Geomorphologie NF Supplementband*, 46, 79-101.
- Sverjensky, D.A., Hemley, J.J., D'Angelo, W.M., 1991. Thermodynamic assessment of hydrothermal alkali feldspar-mica-aluminosilicate equilibria. *Geochim. Cosmochim. Acta.* 55:989-1004
- Takada, K., Nakata, T., Miyagi, T. Haraguchi, T., Nishitani, Y., 2002. Handy Geoslicer –New soil sampler for Quaternary geologist-. *Chishitsu News.* (in Japanese).

- Takarada, S., Oikawa, T., Furukawa, T., Hoshizumi, H., Geshi, N., Itoh, J., Miyagi, I., 2014. Estimation of eruptive total mass of the Sep. 27, 2014 Ontake phreatic eruption. In Abstracts of the Volcanological Society of Japan the 2014 fall meeting, Fukuoka University, Fukuoka, 2-4 Nov. 2014 [in Japanese]
- Takeuchi, M., Nakano, S., Harayama, S., Otsuka, T., 1998. Geology of the Kiso-Fukushima district. With Geological Sheet Map at 1:50,000 Geol. Surv. Japan. (in Japanese, with English Abstr.)
- Uesawa, S., 2014. A study of the Taisho lahar generated by the 1926 eruption of Tokachidake Volcano, central Hokkaido, Japan, and implications for the generation of cohesive lahars. *J. Volcanol. Geotherm. Res.* 270:23-34.
- Ueki, S., Hori, S., 2001. Reexamination of the eruptive activities recorded in history of Chokai volcano. In: Abstracts of the Volcanological Society of Japan the 2001 fall meeting, Kagoshima University, Kagoshima, Japan, pp. 158. [in Japanese]
- Ui, T., Shibahashi, K., 1975. 1974 activity of Chokai volcano, northeastern Japan. *Bull. Volcanol. Soc. Japan*, 20:51-64. (in Japanese, with English Abstr.)
- Vallance, J.W., Scott, K.M., 1997. The Osceola Mudflow from Mount Rainier: sedimentology and hazard implications of a huge-clay-rich debris flow. *Geological Society of America Bulletin* 109:143–163.
- Vallance, J.W., 2000. Lahars. In Sigurdsson, H., Houghton, B.F., McNutt, S.R., Rymer, H., Stix, J. (Eds.), the *Encyclopedia of Volcanoes*. Academic Press, pp. 601-616.
- Vallance, J.W., Iverson, R.M., 2015. Lahars and their deposits. In Sigurdsson, H., Houghton, B., Rymer, H., Stix, J., McNutt, S. (Eds.), the *Encyclopedia of Volcanoes*, second edition. Elsevier, Amsterdam, pp. 649-664.

- Waythomas, C.F., Miller, T.P., Begét, J.E., 2000. Record of Late Holocene debris avalanches and lahars at Iliamna Volcano, Alaska. *J Volcanol Geoth Res.* 104:97-130.
- Xu, S., Ito, S., Iwatsuki, T., Abe, M., Watanabe, M., 2000. A new AMS facility at the JNC Tono Geoscience Center, Japan. *Nucl. Instr. and Meth. in Pys. Res. B*, 172, 8-12.
- Yamada, N., Kobayashi, T., 1988. Geology of the Ontakesan district. With Geological Sheet Map at 1 : 50,000, *Geol. Surv. Japan.* (in Japanese, with English Abstr.)
- Yamamoto T., 1998. Holocene Sukawa lahar deposits at the western foot of Adatara volcano, NE Japan. *Bull. Volcanol. Soc. Japan.* 43:61-68 (in Japanese, with English Abstr.)

ACKNOWLEDGEMENTS

I gratefully acknowledge the discussions and significant technical support rendered by Mr. Sho Komatsu of Okuyama Boring Co., Ltd. and Mr. Mitsugu Handa of Nikaho city. We thank Shinjo Office of River, Tohoku Regional Bureau, MLIT allowing the red relief map to use in this study. I gratefully acknowledge the discussions and significant technical support rendered by Prof. Akira Imai, Prof. Shintaro Hayashi, Dr. Kyoko S. Kataoka, Dr. Yoko Kokubu, Dr. Ryohei Takahashi, Dr. Hinako Sato, Mr. Yushi Ishihara, Mr. Yoshiyuki Yamauchi, Mr. Sho Komatsu, Mr. Handa Mitsugu, and Ms. Yumi Hayakawa. We thank Dr. Kofi Adomako-Ansah and Dr. Jenielyn Tuando Padrones of Akita University for their proofreading of the manuscript. I would like to acknowledge the financial support given by the Akita University Leading Program for Rare Metal Resources. I am also very grateful to the guidance of my supervisor, Prof. Tsukasa Ohba, and the support of my mentors, Dr. Takashi Hoshide and Dr. Taketyki Ogata. I also acknowledge the comments and help of my laboratory mates from the Petrology Laboratory and also the Leading Program students. The Leading Program staff, Ms. Shinogu Suagawara, Ms. Mika Ishioka, Ms. Nobue Shimizu, Ms. Fuyuka Uno, and (former staff) Mr. Ken Fukushima for all the help on Leading Program-related works. This research was supported by Japan Society for the Promotion of Science (JSPS) leading program “New Frontier Leader Program for Rare-metals and Resources” and Japan Society for the Promotion of Science Grant-in-Aid for Scientific Research(C) 15K01245.